Comparing feature maps generated using UNet-like CNN, Transformer, Mamba, and hybrid architectures for general land cover mapping

Aaron E. Maxwell[1*†], Sarah Farhadpour[1†], and Christopher A. Ramezan[2]

[1]West Virginia University Department of Geology and Geography, Morgantown, WV 26505

[2]West Virginia University John Chambers College of Business and Economics, Morgantown, WV 26505

Email: Aaron.Maxwell@mail.wvu.edu (AEM)

[†]Equal contribution

Abstract

This study compares feature maps produced by semantic segmentation architectures using varying combinations of convolutional neural network (CNN), Transformer, and Mamba selective state space (selective SSM) components with a goal of exploring the following question: does correlation or similarity between the generated data abstractions imply comparable predictive performance? Specifically, different encoder and decoder combinations are compared including a fully convolutional neural network (CNN)-based UNet, a Vision Transformer-based Swin-UNet, and a selective state space model (selective SSM)-based Mamba-UNet. For Swin-UNet and Mamba-UNet, we replaced the decoder with a CNN-based architecture comparable to that used within UNet. Central kernel alignment (CKA) and the Mantel test suggest a high degree of similarity between the feature maps generated by the decoder blocks and final feature map representations, respectively; however, the encoder feature maps were more dissimilar. Despite these similarities, differences in model performance were observed. The Mamba-based architectures generally yielded the lowest training losses and highest validation F1-scores. When used as a feature space for traditional machine learning (ML) algorithms, random forest (RF) and support vector machines (SVMs), the Mamba-based feature space generally provided the highest macro-averaged, class-aggregated F1-scores and map image classification efficacies (MICE). Feature reduction from 96 to 15 variables using principal component analysis (PCA), kernel PCA (kPCA), or independent component analysis (ICA) obtained comparable performance in comparison to using the original, larger feature spaces. When provided with all 480 feature maps generated by all five architectures, the Mamba-based features were found to be most important. The study documents that, despite similarities between the final set of feature maps generated by the final decoder block, different architecture combinations yielded varying levels of performance:

similarity between feature spaces did not imply similar predictive performance. Further, we argue that DL-based methods can serve as a means to generate data abstractions for use in traditional ML workflows, and feature reduction can be implemented to reduce the computational load.

Keywords: deep learning; semantic segmentation; land cover classification; convolutional neural networks; Vision Transformers; Mamba; UNet; Swin-UNet; Mamba-UNet

Introduction

Deep learning (DL) techniques for semantic segmentation, or pixel-level labeling, can be conceptualized as architectures that transform input predictor variables, such as image bands, via the learning of spatial patterns. These augmented representations are generally termed feature maps. At a pixel location, the new set of values, or feature space, is used by the classification head, commonly implemented with a linear or 1x1 convolution layer, to predict class labels (Hassaballah and Awad, 2020; Hoeser et al., 2020; Hoeser and Kuenzer, 2020; Maxwell et al., 2026a; Zhang et al., 2023). This is similar to the pixel-level classification performed by traditional machine learning (ML) algorithms, such as random forest (RF) (Breiman, 2001) and support vector machines (SVM) (Cortes and Vapnik, 1995), where the problem can be conceptualized as predicting a class label using a vector of predictor variable values at each pixel location. The key difference is that spatial patterns, textures, and relationships have been “baked” into the augmented feature space using a trainable process and by the prior layers in the architecture (Zhang et al., 2023). This is in contrast to the more traditional incorporation of hand-crafted or user-defined textural measures, such as those generated using the gray-level co-occurrence matrix (GLCM) (Hall-Beyer, 2017; Haralick et al., 1973; Warner, 2011) or via aggregation of individual pixels into homogeneous regions prior to performing the classification, as is implemented with geographic object-based image analysis (GEOBIA) (Blaschke, 2010; G. Chen et al., 2018; Hay and Blaschke, 2010).

Currently, multi-scale and learnable spatial abstractions can be generated via three broad types of DL architectures or a combination of their components. Convolutional neural networks (CNNs), which were widely adopted after 2012, use a combination of trainable kernels, via convolutional layers, and downsampling, via pooling or strided convolution, to learn spatial abstractions at multiple spatial scales (LeCun et al., 2015, 1995). Transformers (Dosovitskiy, 2020; Vaswani et al., 2017), which were adapted for computer vision tasks in 2020 (i.e., Vision Transformers (ViTs)), model relationships between image patches at varying scales using a combination of self-attention and patch merging. Selective state space models (selective SSMs), termed Mamba (Gu and Dao, 2024; Liu et al., 2025), which were first applied to computer vision tasks in 2024 (i.e., VMamba) (Y. Liu et al., 2024), model relationships between image patches using a learned hidden state, patch merging, and by treating patches as sequences generated using different scanning patterns, offering computationally efficient long-range representation learning.

CNNs were first applied to semantic segmentation tasks in 2014/2015 using the fully convolutional network architecture (Long et al., 2015). This architecture was followed by a variety of CNN-based architectures including UNet (Ronneberger et al., 2015), DeepLabv3+ (Chen et al., 2017; L.-C. Chen et al., 2018), UNet++ (Zhou et al., 2019), HRNet (Sun et al., 2019), and UNet3+ (Huang et al., 2020). Example semantic segmentation, transformer-based architectures include Segmenter (Strudel et al., 2021), SegFormer (Xie et al., 2021), Twins (Chu et al., 2021), and Swin-UNet (Cao et al., 2022). There are also hybrid methods that incorporate both CNN- and transformer-based components including TransUNet (Chen et al., 2021) and UNETR (Hatamizadeh et al., 2022). Mamba-based semantic segmentation architectures include Mamba-

UNet (Wang et al., 2024) and U-Mamba (J. Ma et al., 2024). Similar to transformers, hybrid Mamba/CNN architectures have been proposed, including VM-UNet (Ruan et al., 2024) and RS^{3}Mamba (X. Ma et al., 2024). The breadth and rapid evolution in these architectures highlight the continued interest in semantic segmentation methods across domains, including medical imaging, autonomous vehicles, and remote sensing and geospatial science (Hoeser et al., 2020; Hoeser and Kuenzer, 2020; Zhang et al., 2023).

Given that CNN, Transformer, Mamba, and hybrid semantic segmentation architectures are all designed to generate feature maps that capture spatial context important for the classification task of interest, we argue that there is value in exploring and comparing the produced abstractions or representations generated by different architecture combinations, as it remains unclear to what extent these architectures converge toward similar representational structures when trained on the same problem, and whether representational similarity necessarily implies equivalent functional performance. In other words, does similarity between generated representations imply similar predictive performance? We investigate this question within the context of general land cover mapping from high spatial resolution imagery.

We accomplish this by first using central kernel alignment (CKA) (Cortes et al., 2012; Gretton et al., 2005; Kornblith et al., 2019) to quantify the degree of similarity between feature maps generated by all combinations of encoder and decoder blocks constituting pairs of architectures. We also use the Mantel test (Mantel, 1967) to specifically explore the correlation between the final sets of feature maps generated by the final decoder block. The final set of feature maps generated by the last decoder block of each architecture is then provided as an input feature space to traditional ML algorithms, including RF (Breiman, 2001) and SVM (Cortes and Vapnik, 1995) to quantify the impact of the different data abstractions generated on model performance.

We also explore the impact of feature reduction using principal component analysis (PCA) (Jolliffe, 2011), kernel PCA (kPCA) (Schölkopf et al., 1998), and independent component analysis (ICA) (Hyvärinen et al., 2001). Lastly, feature variable importance is explored using RF-, permutation-based methods (Debeer and Strobl, 2020) to identify which architecture-derived representations contribute most strongly to predictive performance.

We explore UNet (Ronneberger et al., 2015) with a ResNet-34-based encoder (He et al., 2015), a fully CNN-based architecture, Swin-UNet (Cao et al., 2022), a fully Transformer-based architecture, and Mamba-UNet (Wang et al., 2024), a fully Mamba-based architecture. We then augment both Swin-UNet and Mamba-UNet by replacing the decoder with a CNN-based decoder comparable to the one used within UNet. The five architectures explored, along with the abbreviations used in the study and count of trainable parameters, giga floating point operations (gFLOPS), and giga multiply-accumulate operations (gMACs), are provided in Table 1. We did not prioritize comparing the most recently released architectures; instead, we selected architectures that have a similar "U"-shaped design for a consistent comparison. For an example extent, images of all 96 feature maps generated by the last decoder block of all five architectures, or a total of 480 feature maps, have been provided as a supplement to this study.

Table 1. Model architectures explored in this study including used abbreviations and a comparison of model architecture parameter counts and computational load. gFLOPS = giga floating point operations; gMACs = giga multiply-accumulate operations.

Architecture	Encoder Type	Decoder Type	Abbreviation Used In Study	Trainable Parameter Count	gFLOPS	gMACs
UNet (ResNet-34)	CNN	CNN	UNet	48,973,477	872.78	436.12
Swin-UNet	Transformer	Transformer	SwinUNet	41,380,452	139.03	69.21
-	Transformer	CNN	SwinUNetC	55,532,393	321.68	160.62
Mamba-UNet	Mamba	Mamba	MambaUNet	19,121,760	71.85	27.91
-	Mamba	CNN	MambaUNetC	47,485,637	308.18	149.69

Background

Convolutional neural networks (CNNs) and UNet

CNN architectures make use of convolutional filters or kernels to generate spatial abstractions of the input data (LeCun et al., 2015, 1995; Zhang et al., 2023). During the training process, the weights that constitute the kernels and a bias or shifting term per kernel are updatable. Smaller windows sizes are commonly used to capture local textures and patterns and also to minimize the number of trainable parameters, computational load, and risk of overfitting; as a result, the receptive field is small, which practically results in a limited ability to characterize broader-scale spatial patterns or more global spatial context. This issue is partially alleviated by incorporating pooling operations or strided convolution as a means to reduce the spatial resolution of feature maps. Subsequent convolutional layers are then applied to these spatially coarser representations, which allows for a small window, such as a 3x3 window, to capture broader spatial context but at the cost of reduced spatial detail (Zhang et al., 2023).

UNet is a CNN-based architecture designed for semantic segmentation, or pixel-level classification. The encoder component captures spatial context information at varying spatial scales. In the original UNet implementation, each block in the encoder, termed a double-convolution block, contains two 3x3 2D convolution operations, which are each followed by a batch normalization layer, which normalizes the output data within each processed mini-batch to enhance training stability (Ioffe and Szegedy, 2015; Luo et al., 2018; Santurkar et al., 2018), and a rectified linear unit (ReLU) activation function (Nwankpa et al., 2018; Sharma et al., 2017), which adds nonlinearity (Ronneberger et al., 2015). Within the encoder, 2x2 2D max pooling is used to reduce the size of the feature maps between encoder blocks in the spatial dimensions and allow for modeling spatial context at varying spatial scales. The bottleneck is the stage of the architecture between the encoder and decoder at which the feature maps reach their smallest size in the spatial dimensions but contain the highest degree of semantic information. The decoder then restores the spatial resolution of the feature maps in the spatial dimensions using 2x2 2D transpose convolution while further augmenting the representations using double convolution blocks. The final set of feature maps are passed to the classification head, which uses 1x1 2D convolution to transform the final set of feature map values at each cell location to predicted class logits. Another key component of UNet architectures is the use of skip connections between encoder and decoder blocks with the same spatial resolution. This reduces the semantic gap between the encoder and decoder (Ronneberger et al., 2015).

The augmented version of UNet used in this study is conceptualized in Fig 1. We made two key augmentations. First, the traditional double-convolution blocks of the encoder were replaced with residual convolution blocks from the ResNet-34 architecture (He et al., 2015). The number of residual blocks used in each encoder block are noted in the figure. ResNet uses strided convolution to reduce the spatial resolution of the feature maps, and a max pooling layer is only used after the first convolution operation. Since the first convolution block also uses strided convolution, the resolution of the data is reduced by a factor of two in the first encoder block. As a result, the final output from the decoder must be upsampled before being provided to the classification head. We also replaced the ReLU activation functions in the decoder with leaky ReLU, which maintains negative activation values but with a reduced magnitude (Nwankpa et al., 2018; Sharma et al., 2017).

[INSERT FIGURE 1]

Fig 1. UNet with a ResNet34 encoder. w = width; h = height; E = encoder; B = bottleneck; D = decoder.

Vision Transformers (ViTs) and Swin-UNet

In comparison to CNNs, ViTs (Dosovitskiy, 2020) use a fundamentally different means to model spatial patterns and context. The key component of these architectures is the multi-head self-attention mechanism, which supports the modeling of relationships between patches of cells within an example image. Transformer architectures were originally developed for natural language processing where each word or unit is represented as a token. To augment this framework for image tasks, a means to segment an image into tokens is required. This is generally accomplished by first segmenting the image into subset regions using patch partitioning. Here, we used 4x4 regions, which is common for semantic segmentation tasks. These patches serve as individual tokens. The cell values within each token are converted to a 1-dimensional vector and then to an embedding of a predefined length using a linear or fully connected layer. The relationships between these patches are then modeled using the multi-head self-attention mechanism. Multiple heads of self-attention are used so that each head can focus on different semantic information (Dosovitskiy, 2020).

Swin-UNet (Cao et al., 2022), which was used in this study, is conceptualized in Fig 2(a). In comparison to traditional UNet, CNN-based, double-convolution blocks in the encoder, bottleneck, and decoder are replaced with two shifted window (swin) self-attention blocks (Liu et al., 2021). These blocks do not use global attention; instead, attention is applied within local, fixed-size windows. The first Transformer component within each block uses non-overlapping windows (W-MSA or window-based multi-head self-attention) while the second uses windows that overlap (SW-MSA or shifted window-based multi-head self-attention), which is accomplished by shifting the window by a factor smaller than the window size. This allows for sharing of information between the windows. These blocks also use layer normalization, multilayer perceptron (MLP) layers, and residual connections (Cao et al., 2022). We also paired a Swin-Transformer-based encoder with a CNN-based decoder (SwinUNetC), as conceptualized in Fig 2(b). This decoder mirrors the one used within the CNN-based UNet (Fig 1).

[INSERT FIGURE 2]

Fig 2. Swin-UNet architecture used in this study with a Swin-Transformer-based encoder and decoder (SwinUNet) (a) and a Swin-Transformer-based encoder and CNN-based decoder (SwinUNetC) (b). w = width; h = height; E = encoder; B = bottleneck; D = decoder; U = upsample.

Instead of using max pooling operations, spatial resolution is commonly reduced using patch merging, which groups 2x2 regions of neighboring patches. The reduction in the resolution, or number of tokens, reduces the computational load, which decreases the computational demand associated with using a longer embedding length. In order to increase the spatial resolution in the decoder, patch expansion is used as opposed to transpose convolution. This is accomplished by increasing the length of the embedding then reshaping the data to reduce the number of channels and increase the length of the spatial dimensions (Dosovitskiy, 2020).

Since the patch embedding operation uses a 4x4 cell patch size, the first encoder block receives an input that has already had its spatial dimensions reduced by a factor of four. After passing through three encoder blocks and the bottleneck, the spatial resolution is decreased by a factor of 32. Patch expanding operations in the decoder restore the original spatial resolution. As with the CNN-based UNet, skip connections are added between encoder and decoder blocks. Note that a skip connection is not used with the final decoder block since there is no encoder block with the same size in the spatial dimensions (Cao et al., 2022).

Mamba and Mamba-UNet

The underlying concept behind Mamba (Gu and Dao, 2024) is maintaining important information within an evolving hidden state while discarding irrelevant information, which contrasts with multi-head self-attention that attempts to model all relationships between all elements regardless of importance. The current hidden state (h_t) depends on the prior hidden state (h_t-1) and the current input (x). Learnable matrix A captures how to transition the current state into the next state while matrix B captures key information about the input in regard to how it should modify the hidden state. Since the goal is not to predict the next hidden state but an output, matrix C is used to map the hidden state to the output of interest. It is also common to use a projection of the input data, via matrix D, as a skip connection. To modify the problem from a continuous-time to a discrete-time process requires discretization of the input data, which is conceptualized as a model time step or how fast the hidden state evolves. One key component of this architecture is its selective nature: the hidden state and output are impacted by the input data. In other words, the state transition and output matrices are functions of the input, enabling efficient long-range modeling with linear complexity (Gu and Dao, 2024).

Similar to ViTs for Transformers, VMamba (Liu et al., 2025) augments Mamba for vision tasks using a vision state space (VSS) block. In Transformer-based architectures, such as the Swin-Transformer block described above, linear or fully connected layers are used to perform computation on a token's associated embeddings while multi-head self-attention is used to capture relationships between tokens, which, is computationally expensive. VSS blocks still use linear layers to perform computation or modification of the token embeddings; however, the between-token communication component makes use of the computationally lighter SSM (Gu and Dao, 2024). Also similar to ViTs, this requires treating patches of cells within image extents as tokens, which are associated with embeddings (Liu et al., 2025). The 2D selective scan (SS2D) module is a key component of the VSS block. Patches are treated as records within a sequence, and different sequences are generated using different scanning patterns, as implemented with the cross-scan module. Relationships within each sequence are modeled using separate S6 blocks, and information between the different scanning patterns are then merged by the cross-merge module (Liu et al., 2025).

Mamba-UNet (Wang et al., 2024) is conceptualized in Fig 3(a). Similar to Swin-Transformer-based architectures, image data must be transformed into tokens, and this is accomplished using patch merging and linear embeddings. Downsampling is accomplished using patch merging while upsampling is accomplished using patch expansion. Due to generating the initial patches using 4x4 patches of cells, the input to the first encoder block has one-fourth the spatial resolution of the input data, and additional patch expansion is used in the decoder to obtain the prediction at the original spatial resolution (Wang et al., 2024). The key difference between Swin-UNet and Mamba-UNet is that the double Swin-Transformer blocks are replaced with double VSS blocks (Wang et al., 2024). As with the Transformer-architecture, we also replace the decoder with a CNN-based decoder (MambaUNetC) (Fig 3(b)) for this study.

[INSERT FIGURE 3]

Fig 3. Mamba-UNet architecture used in this study with a VSS-based encoder and decoder (MambaUNet) (a) and a VSS-based encoder and CNN-based decoder (MambaUNetC) (b). w = width; h = height; E = encoder; B = bottleneck; D = decoder; U = upsample.

Methods

Example dataset

In this study, we used the LandCover.ai (version 1) dataset (Boguszewski et al., 2021), which consists of high spatial resolution RGB images for areas within Poland along with complete manually annotated, pixel-level labels that differentiate five classes: background, buildings, woodlands, water, and roads. Specifically, the dataset consists of 33 orthophotos at 25 cm spatial resolution and eight orthophotos at 50 cm spatial resolution covering a total area of 216 km^2. The dataset spans diverse rural landscapes and includes scenes acquired under varying illumination, atmospheric conditions, and seasonality (Boguszewski et al., 2021). We selected this dataset due to its high spatial resolution but limited number of spectral bands. In RGB-only settings, spectral separability is limited, therefore textures, spatial patterns, and contextual relationships are critical for class discrimination.

We adopted the non-overlapping 512×512 training, validation, and testing splits defined by the dataset authors and randomly sampled, without replacement, 5,000 image chips for training, 1,600 for validation, and 1,600 for testing. As part of preprocessing, we applied probabilistic data augmentation to the training set to combat overfitting. Horizontal and vertical flips were each applied with a 50% probability per image, median blurring was applied with a 10% probability (blur limit = 3), and random brightness/contrast adjustment were applied with a 50% probability (brightness limit = 0.3, contrast limit = 0.3). In addition, we performed a center crop on the training, validation, and test sets, extracting the central 224×224 region from each chip to match the input-size requirements of the Swin- and Mamba-based architectures evaluated in this study. The same preprocessing and augmentation pipeline was applied across all architectures to ensure a consistent comparison.

Architecture generation and training process

Model training was performed in Python ("Welcome to Python.org," n.d.) using the PyTorch deep learning framework ("PyTorch," n.d.). GPU-based acceleration was implemented using the Compute Unified Device Architecture (CUDA) ("CUDA Toolkit - Free Tools and Training," n.d.) and the cuDNN library ("CUDA Deep Neural Network (cuDNN) | NVIDIA Developer," n.d.).

The baseline UNet was implemented using the Segmentation Models library (Iakubovskii, 2019) with minor modifications to use the leaky ReLU activation function in the decoder as opposed to ReLU. Swin-UNet (SwinUNet) and Mamba-UNet (MambaUNet) were implemented using the original open-source code released by their developers (Cao et al., 2022; Wang et al., 2024). The hybrid variants, SwinUNetC and MambaUNetC, were generated by the authors of this study using PyTorch and the original SwinUNet and MambaUNet code.

All models were trained for 25 epochs with a mini-batch size of eight. We used the AdamW optimizer with a learning rate of 1e-4 applied uniformly across trainable parameters and optimized using Dice loss to mitigate the effects of class imbalance. All encoders were initialized using ImageNet-based weights (Deng et al., 2009); however, they were unfrozen or updatable during the training process. We selected the epoch checkpoint achieving the highest validation F1-score during training as the final model.

Central kernel alignment (CKA) and Mantel test

CKA was used to compare the similarity between two sets of values or representations. It generates a scalar value between 0 and 1 for all compared elements, such as all combinations of evaluated layer outputs between two models. It first uses a kernel function to project the data into a higher dimensional feature space. Within this higher-dimensional space, the Hilbert-Schmidt independence criterion (HSIC) is calculated, which serves as a measure of dependence between two sets of values. CKA augments HSIC using normalization in order to make it scale invariant. CKA is invariant to orthogonal transformations, isotropic scaling, and mean shifts (Cortes et al., 2012; Gretton et al., 2005; Kornblith et al., 2019). We used this method to perform a pairwise comparison of all combinations of the five tested model architectures. We specifically compared the feature map outputs of each encoder block, the bottleneck, and each decoder block. Our goal was to generally assess the level of similarity between the feature maps generated at different stages in the investigated architectures.

To evaluate the degree of structural similarity among feature representations generated by the last decoder block from each of the five segmentation architectures, pairwise comparisons were conducted using the Mantel test (Mantel, 1967) as implemented in the vegan package (Oksanen et al., 2026) in R. For each class, a stratified random sample of 500 pixels per class label was drawn from the full training set to ensure balanced class representation while keeping the comparison computationally tractable. Feature map values were scaled to zero mean and unit variance and used to compute a cross-product (Gram) matrix for each model, capturing the pairwise similarity structure among sampled locations within that model's feature space. Mantel tests (999 permutations) were then run on all pairwise combinations of these matrices to assess whether the similarity structure encoded by one model's feature space corresponded to that encoded by another, with statistical significance assessed via permutation rather than a parametric null distribution to account for the non-independence of matrix entries. Because the Mantel test was applied to cross-product matrices rather than conventional Euclidean distance matrices, this analysis is mathematically equivalent to a permutation test of the RV coefficient. A high and significant Mantel correlation, generally above 0.50, between two models' feature spaces would indicate that the two architectures organize the sample locations in a structurally similar way, despite differences in network design, while low or non-significant correlations would suggest the two models capture substantially different aspects of the underlying data (Mantel, 1967).

Machine learning models and assessment

The RF and SVM classification models were trained using the tidymodels environment (Kuhn and Wickham, 2020) in the R language (R Core Team, 2025). For this study, the tidymodels framework made use of the ranger (Wright and Ziegler, 2017) and kernlab (Karatzoglou et al., 2004) packages to implement the RF and SVM algorithms, respectively. At 640,000 randomly selected pixel locations from the training set chips, or 128 pixel locations within each of the 5,000 training chips, we extracted the final set of 96 feature map values generated by each of the five architectures, or a total of 480 values, along with the reference class label. From this large set, we randomly selected 1,000 examples of each of the five classes for a total of 5,000 training samples. For assessment and from the test set, we selected 128 random pixel locations from each of the 1,600 chips, or a total of 204,800 samples. We then randomly selected 10,000 examples from the larger set. In contrast to the training set, we did not use stratified random sampling in order to maintain the relative class proportions from the large set of test set pixels.

Model tuning was conducted using ten-fold cross validation and a grid search consisting of 25 values for each hyperparameter. For RF, 500 trees were used, and we tuned the number of randomly selected predictor variables to select from at each node (*mtry*) and the minimum number of data points in a node that are required for the node to be split further (*min_n*) hyperparameters. For SVM, a radial basis function (RBF) kernel was used, and the *cost* and *sigma* hyperparameters were tuned. A total of four models were trained for each of the five architectures using either the original input feature space or 15 new features generated using PCA, kPCA, or ICA. Feature reduction was undertaken using the recipes package (Kuhn et al., 2024). The hyperparameters that provided the highest mean macro-averaged F1-score across withheld folds were selected as the final settings, and these settings were then used to train final models using the entire training set. Models were assessed using the micer R package (Maxwell and Farhadpour, 2025) and the randomly selected test pixels. Overall accuracy (OA) (Equation 1) represents the proportion of samples correctly classified. Macro-averaged, class aggregated precision (Equation 2) and recall (Equation 3) represent 1 − commission error and 1 − omission error, respectively, calculated such that each class has equal weight in the aggregated metric. The macro-averaged F1-score (Equation 4) represents the harmonic mean of these two measures (Maxwell et al., 2026b). Equations 2 through 4 are defined relative to class-level true positive (TN), false positive (FP), and false negative (FN) counts. These counts are calculated separately for each class (*j*) for all classes (*C*) then divided by the number of classes (*N*). Map image classification efficacy (MICE) (Shao et al., 2021; Tang et al., 2024) offers and adjustment of OA relative to a random classification baseline (OA_0) (Equation 5). For class *j*, the probability that a random sample is correctly labeled to that class is equivalent to the square of the proportion of the total count of samples, *n*, that belong to class *j* (n_j). The estimated accuracy of a random classification is defined as the sum of all these class-level probabilities, and OA is adjusted to obtain MICE by subtracting OA_0 and dividing by $1 - OA_0$ (Equation 6) (Shao et al., 2021; Tang et al., 2024). For all assessment metrics, we estimated 95% confidence intervals using bootstrap sampling of the test set samples and 1,000 replicates.

$$\text{Overall accuracy (OA)} = \frac{\text{Count of correctly classifed samples}}{\text{Total count of samples}} \text{ (Equation 1)}$$

$$\text{Macro-averaged, class aggregated precision} = \frac{1}{N}\sum_{j=1}^{C}\frac{\text{TP}_j}{\text{TP}_j + \text{FP}_j} \text{ (Equation 2)}$$

$$\text{Macro-averaged, class aggregated recall} = \frac{1}{N}\sum_{j=1}^{C}\frac{\text{TP}_j}{\text{TP}_j + \text{FN}_j} \text{ (Equation 3)}$$

$$\text{Macro-averaged, class aggregated F1-score} = \frac{1}{N}\sum_{j=1}^{C} \frac{2\times \mathrm{TP}_j}{2\times \mathrm{TP}_j + \mathrm{FN}_j + \mathrm{FP}_j} \text{ (Equation 4)}$$

$$\text{Accuracy of a random classification } (\mathrm{OA}_0) = \sum_{j=1}^{C} \left(\frac{n_j}{n}\right)^2 \text{ (Equation 5)}$$

$$\text{Map image classification efficacy (MICE)} = \frac{OA - OA_0}{1 - OA_0} \text{ (Equation 6)}$$

Other than assessing the impact of feature reduction on classification performance using 15 components calculated with PCA, kPCA, or ICA, as described above, we also explored the percentage of total variance in the original 96 feature map values explained by these components when generated using PCA or kPCA. This analysis aimed to explore the potential for reducing the large set of 96 feature maps to a smaller set to potentially reduce the computational load of storing a large number of predictor variables if the DL architecture is used as a feature extraction framework to provide input predictor variables to a traditional ML model.

Feature importance

Lastly, we trained an RF-based model using all 480 feature map values from all five models then assessed the importance of individual variables within this large feature space. Other than as a classification algorithm, RF has generally been adopted as a framework for assessing the importance or contribution of predictor variables (Breiman, 2001; Gregorutti et al., 2017; Maxwell et al., 2026c). However, there are known biases with the traditional RF implementation when there is correlation between continuous predictor variables (Debeer and Strobl, 2020; Strobl et al., 2008, 2007). As a result, we used an augmented variable importance estimation method that takes into account correlation between predictor variables as implemented in the permimp R package (Debeer et al., 2021). In this study, the algorithm was configured to obtain an estimate of marginal as opposed to conditional importance. Marginal importance is meant to assess the importance of the variable regardless of the other predictor variables included in the model as opposed to the added value of the variable within the current feature space (Debeer and Strobl, 2020).

Results

Model training

Fig 4 shows the model training results per epoch for the training loss (Fig 4(a)) and the validation set macro-averaged F1-score (Fig 4(b)) while Fig 5 shows an example image extent (a), reference labels (b), and all classification results (c through g). MambaUNet and MambaUNetC stabilized at the lowest training loss and highest validation F1-scores. UNet and SwinUNetC generally showed intermediate performance while SwinUNet stabilized at the highest training loss and lowest validation F1-score. The model training results generally suggest strong performance for the Mamba-based architectures and that using a CNN-based decoder generally did not harm model performance for the Mamba-based architecture and improved performance for the Swin-Transformer-based architecture. The visualizations of the results provided in Fig 12 generally suggest errors are most prominent for thin or small features, such as roads and buildings, and along class margins for all models.

[INSERT FIGURE 4]

Fig 4. Model training losses (a) and validation F1-scores (b) across all 25 training epochs for all five architectures.

[INSERT FIGURE 5]

Fig 5. Example classification results. (a) input image; (b) reference data; (c) UNet result; (d) Swin-UNet result; (e) Swin-UNetC result; (f) Mamba-UNet result; (g) Mamba-UNetC result.

CKA and Mantel test

The CKA results are shown in Fig 6. As noted above, we focused on comparing the final feature map representations produced by each encoder, bottleneck, or decoder block, as opposed to other intermediate representations. Each matrix represents a pair of architectures being compared. Higher representational similarity (CKA > 0.80) was consistently observed between corresponding decoder blocks, whereas encoder and bottleneck blocks exhibited lower similarity (typically < 0.75). This pattern persisted even when the same encoder architecture was used (e.g., SwinUNet vs. SwinUNetC; MambaUNet vs. MambaUNetC). A notable exception was the representations produced by the very first encoder block, which generally showed high degrees of correlation between SwinUNet and SwinUNetC or MambaUNet and MambaUNetC. For the same problem, general land cover mapping, and when using the same training set, the decoder generally learned similar representations even when receiving input representations from different encoders (i.e., CNN-based ResNet-34, Mamba, or Swin-Transformer). Further, even when using the same, CNN-based decoder architecture, representations learned by different encoder architectures were generally more variable. One possible explanation is that different decoder architectures may require different input feature map representations from the encoder, since, during backpropagation, the "signal" must pass through some or all decoder blocks when calculating gradients with respect to encoder parameters. It is notable that, despite the high degree of correlation between generated feature maps in the decoder, that the training curves presented in Fig 4 above generally suggest differences in model performance and generalization to the validation set. In other words, despite similarities, the final set of feature maps passed to the classification head from the final decoder block did not yield the same level of performance.

[INSERT FIGURE 6]

Fig 6. CKA results for comparing pairs of models for outputs from each encoder, bottleneck, and decoder block.

The Mantel test results generally support those obtained using CKA. All pairwise comparisons were statistically significant at the 95% confidence level, and all Mantel r values were above 0.5. The UNet architecture was generally more correlated with the SwinUNetC and MambaUNetC architectures, or those using a CNN-based decoder, than those not using a CNN-based decoder: SwinUNet and MambaUNet. MambaUNet was most highly correlated with MambaUNetC, suggesting similarities between the feature maps generated by the final decoder block despite using a Mamba-based as opposed to CNN-based decoder. There was also a strong correlation between SwinUNet and SwinUNetC. Despite the differences in validation performance as highlighted in Fig 4(b) above, the SwinUNet feature maps showed similarity with those generated using the two architectures incorporating Mamba-based components.

Table 2. Mantel r values for pairwise comparisons between the final feature space of 96 feature maps per architecture calculated using a random subsample of pixel locations (stratified sample of 500 pixels for each class or a total of 2,500 pixels). All pairwise comparisons were statistically significant at the 95% confidence level.

	SwinUNet	SwinUNetC	MambaUNet	MambaUNetC
UNet	0.6708	0.7042	0.6858	0.7002
SwinUNet		0.705	0.7234	0.6615
SwinUNetC			0.7535	0.7178
MambaUNet				0.7411

ML-based prediction and feature reduction

Fig 7 summarizes the classification results obtained using the RF and SVM algorithms for the five calculated assessment metrics and for each of the five architectures explored when using the original 96 feature map values or 15 components calculated using PCA, kPCA, or ICA. The results obtained with the two traditional ML algorithms generally mirror those obtained with the DL models reported above: the MambaUNet and MambaUNetC models generally provided the highest mean F1-scores and MICE values across bootstrap replicates while SwinUNet yielded the poorest performance. For MambaUNet, and when using the original feature map values and the RF algorithm, a mean F1-score of 0.787 and a mean MICE of 0.832 were obtained. When using the SVM algorithm, a mean F1-score of 0.810 and a mean MICE of 0.848 were obtained. In contrast, SwinUNet yielded mean F1-scores of 0.737 and 0.769 and MICE values of 0.762 and 0.809 when using RF and SVM, respectively. The UNet and SwinUNetC results were intermediate.

Using a CNN-based decoder generally improved performance when using the Swin-Transformer-based encoder (SwinUNetC) (RF F1-score = 0.786; SVM F1-score = 0.787; RF MICE = 0.817; SVM MICE = 0.818) and slightly improved performance when using a Mamba-based encoder (MambaUNetC) (RF F1-score = 0.817; SVM F1-score = 0.828; RF MICE = 0.840; SVM MICE = 0.853). Mean OA scores were generally high, which we attribute to class imbalance. Specifically, the water, road, and building classes constitute small percentages of the landscape in comparison to background and woodlands. The macro-averaged, class-aggregated metrics are more meaningful in this context.

[INSERT FIGURE 7]

Fig 7. Accuracy assessment comparison of different feature spaces when using the RF and SVM algorithms. Red dots represent mean values while bars indicate the 95% confidence interval calculated using 1,000 bootstrap replicates.

As highlighted in Fig 8, there was some correlation between the difference in F1-score and MICE and the associated Mantel r values for model pairs: a negative trend was observed, suggesting that less similar feature spaces tended to yield more disparate assessment metric values.

The correlations were stronger for RF than SVM; however, all R^2 values for linear trend lines were <= 0.30. In other words, a negative correlation was noted, but the fit was weak.

[INSERT FIGURE 8]

Fig 8. Mantel r and absolute difference in F1-score and MICE values for model pairs obtained using the RF and SVM algorithms.

Reducing the feature space from the original 96 feature map values to 15 components using PCA, kPCA, or ICA generally did not reduce model performance. For example, for MambaUNetC, the mean F1-score when using the original feature space and RF algorithm was 0.817 while it was 0.817, 0.817, and 0.818 when using 15 components calculated with PCA, kPCA, or ICA, respectively. For MambaUNetC and when using the SVM algorithm, the mean F1-scores were 0.828, 0.828, 0.827, and 0.828 for the original, PCA, kPCA, and ICA feature spaces, respectively.

Fig 9 provides Scree plots for the first 15 principal components for the PCA results while Fig 10 provides the same information for the kPCA results. The bars represent the percentage of total variance explained by each component, and the percentage is labeled for all components explaining greater than 1% of the total variance. The results suggest that the total variance in the set of 96 feature map values generated by the last decoder block could generally be captured by a relatively small number of principal components. However, more principal components were needed when using a CNN-based decoder (Figs 9(a), (c), and (e) and Figs 10(a), (c), and (e)) as opposed to a Swin-Transformer or Mamba-based decoder (Figs 19(b) and (d) and Figs 10(b) and (d)). For both SwinUNet and MambaUNet, the first four principal components for PCA captured nearly all of the variance in the original variables (98.3% for SwinUNet and 97.0% for MambaUNet) while more components were needed when using the CNN-based decoders. For example, 88.4%, 79.0%, and 88.1% of the total variance was captured by the first four components for UNet, SwinUNetC, and MambaUNetC, respectively. The kPCA-based feature reduction (Fig 10) generally required more components than the PCA results (Fig 9) to capture the same amount of total variance. For example, the first four principal components for UNet when using kPCA captured 41.5% of the total variance while the PCA result captured 88.4%. This difference arises because kPCA performs dimensionality reduction in a nonlinear, implicitly mapped feature space, and the variance explained is computed in that transformed space rather than directly in the original linear feature space. The reason for the differences between the CNN-based decoder and Swin-Transformer- or Mamba-based decoder is not known and merits further investigation. Perhaps the smaller receptive field of the convolution blocks in the CNN-based decoder results in more variability amongst the generated feature maps whereas the larger context of the Swin-Transformer or VSS blocks results in capturing less variable patterns.

[INSERT FIGURE 9]

Fig 9. Scree plot of total variance of the output feature maps explained by the first 15 principal components for each architecture configuration. Components that explain more than 1% of the total variance are labeled.

[INSERT FIGURE 10]

Fig 10. Scree plot of total variance of the output feature maps from each model explained by the first 15 kernel principal components for each architecture configuration. Components that explain more than 1% of the total variance are labeled.

RF-based importance estimation

Fig 11 shows the distribution of estimated marginal importance values for the highest ranked 25 predictor variables when using all 480 feature maps based on correlation-corrected, permutation-based importance and the RF algorithm. Fig 12 provides visualizations of the eight top-ranked feature maps for an example extent. As noted above, all 480 feature maps for this same extent are provided as an supplement to this study. The top ranked 25 feature maps were either generated by the MambaUNet or MambaUNetC architecture. More specifically, 16 feature maps were from the MambaUNetC model while nine were from the MambaUNet model. These results suggest that, when provided with feature maps from all five architectures, those generated by architectures incorporating Mamba were generally found to be most useful. However, a large proportion of feature maps generated by MambaUNetC, which used a CNN-based decoder, were found to be important. Fig 13 shows the distribution of importance ranks for the set of feature maps provided by each architecture. Feature maps generated by MambaUNetC had the lowest median rank; however, there was more variability in ranks in comparison to MambaUNet. SwinUNet, similar to the DL training and ML algorithm assessment results reported above, generally yielded feature maps that were not highly ranked as important while UNet and SwinUNetC ranks were intermediate. The use of a CNN-based decoder alongside a Swin-Transformer-based encoder (SwinUNetC) yielded improved performance ranks in comparison to a purely Swin-Transformer-based architecture (SwinUNet).

[INSERT FIGURE 11]

Fig 11. Estimate of the 25 most important predictor variables for an RF model trained with all 480 feature maps. Marginal variable importance was estimated using correlation-adjusted, permutation-based methods and the permimp R package (Debeer et al., 2021).

[INSERT FIGURE 12]

Fig 12. Eight highest ranked feature maps (see Fig 11).

[INSERT FIGURE 13]

Fig 13. Distribution of feature map importance ranks for each model architecture. Marginal variable importance was estimated using the RF algorithm and correlation-adjusted, permutation-based methods within the permimp R package (Debeer et al., 2021).

Discussion

We explored the feature maps, or spatial abstractions, generated by different UNet-like architectures. Specifically, we explored a CNN-based UNet, a ViT-based Swin-UNet, and a selective SSM-based Mamba-UNet. We also replaced the decoders for Swin- and Mamba-UNet with a CNN-based decoder comparable to that used within UNet. CKA documented a high degree of similarity between the feature maps generated by the decoder blocks across all pairs of model architectures. Lower degrees of similarity were noted between the encoder blocks and bottleneck block. This was true even for models using the same encoder but a different decoder (i.e., MambaUNet vs. MambaUNetC or SwinUNet vs. SwinUNetC). Importantly, the results suggest that the final set of feature maps generated by the final decoder block and passed to the classification head generally capture similar information. All pairs of final decoder blocks had CKA values above 0.88 and Mantel r values above 0.65. It has generally been documented that CNN- and Transformer-based architectures generally "see" differently, which is commonly attributed to the limited receptive field of CNN architectures, especially in earlier layers of the model architecture (Raghu et al., 2021). Despite this, our results suggest that later stages of the architectures may generate output with a high degree of similarity.

However, convergence in representational similarity did not translate into equivalent optimization dynamics or generalization performance. Although decoder-level feature maps appeared highly aligned under CKA, and the final decoder block outputs showed alignment for both CKA and Mantel r, the models exhibited meaningful differences in training behavior and downstream classification results. CKA measures alignment between feature spaces but does not capture differences in class separability, margin structure, calibration, or robustness. Even subtle variations in how representations are distributed within a similar learned feature space may influence predictive performance. These findings suggest that architectural inductive biases continue to shape functional classification outcomes, even when final decoder feature maps appear highly similar.

Consistent with this interpretation, the Mamba-based architectures (MambaUNet and MambaUNetC) generally reached lower training losses and higher validation F1-scores in comparison to the other architectures. When the final set of 96 feature maps generated by each of the five architectures were provided to the RF or SVM traditional ML algorithm, the Mamba-based feature spaces generally provided the strongest performance, as measured with class-aggregated, macro-averaged F1-score and MICE. When an RF algorithm was provided with all 480 feature maps, the Mamba-based features were generally found to be most important.

One potential reason for the poorer performance of the transformer-based architecture (SwinUNet) is the limited sample size, as prior studies have documented that ViTs may underperform CNNs when the training set size is small. This is sometimes attributed to the lack of inductive bias inherent to ViTs [16,75–78]. This could further explain why using a Swin-transformer-based encoder and a CNN-based decoder (SwinUNetC) generally improved performance relative to a purely transformer-based architecture (SwinUNet) in this specific study. There is currently less research documenting the impact of training sample size on Mamba-based models; however, Mamba-focused papers have noted the computational cost and training data requirements of Transformers as a reason to develop alternative architectures [18,20,34]. This study generally suggests strong performance of Mamba architectures, even with a limited sample size and when initializing the encoder with pre-trained weights while also supporting prior research that suggests Transformer-based architectures may not be the optimal choice when sample size is limited.

Hybrid architectures that use a Mamba- or Transformer-based encoder and a CNN-based decoder generally performed well in this study. SwinUNetC outperformed SwinUNet, and slight improvements were noted when comparing MambaUNetC to MambaUNet. Generally, the highest performing architecture explored in this study was MambaUNetC. With limited sample size, our results suggest that using a hybrid architecture may improve performance. Several hybrid Transformer/CNN or Mamba/CNN architectures have been proposed, and the authors of these architectures have argued for the value of hybrid designs (e.g., [32,33,37,79]). For example, RS^3Mamba [37], which was developed for use in remote sensing tasks, includes a dual-branch encoder, one using VSS blocks and one using residual CNN blocks, and a CNN-based decoder. The encoder also uses a collaborative completion module (CCM), which incorporates Transformer-based components, to combine information between the dual branches [37].

DL semantic segmentation architectures, as noted above, can be conceptualized as a means to generate spatial abstractions guided by the classification task of interest. The feature maps generated by the final decoder block serve as an input feature space for the pixel-by-pixel classification performed by the classification head. This study suggests that these feature spaces can also serve as input for more traditional ML-based classification algorithms and workflows. Further, feature reduction, as performed using PCA, kPCA, or ICA, can be used to generate a smaller set of features from a large set of feature maps without reducing classification performance. There is some notable value in being able to perform classifications using ML-based methods. First, these methods are generally computationally lighter than DL-based methods and can be performed using CPU-based, as opposed to GPU-based, computation. There are also excellent tools available to tune, train, and compare models, such as the tidymodels metapackage [61] in R. It is also possible to improve performance by using model ensembles [80]. We suggest that there is a need to further explore hybrid workflows that use DL architectures to generate augmented feature spaces as input to ML-based algorithms. For example, a pre-trained semantic segmentation architecture could be used to generate a feature space that is then reduced in dimensionality using PCA, kPCA, or ICA. This reduced feature space could then serve as input to a ML-workflow. Large foundation models, such as AlphaEarth [81], have recently been introduced that generate feature spaces or embeddings from input remotely sensed data to serve as predictor variables in downstream modeling tasks. We argue that there is a need to develop foundation models specific to commonly used input spaces, such as high spatial resolution RGB orthophotography, to generate feature spaces for ML-based high spatial resolution land cover mapping.

Conclusions

This study explored the feature map representations generated by CNN, Transformer, Mamba, and hybrid semantic segmentation architectures. Three primary findings emerged. First, decoder-level feature maps generated by different architectures exhibited a high degree of similarity despite differences in encoder representations. Second, variability in classification performance was observed despite this representational similarity, indicating that similarity in learned feature spaces does not necessarily correspond to equivalent predictive performance. Third, the final set of feature maps generated by the last decoder block can be repurposed as input feature spaces for traditional ML workflows.

Of the architectures explored, the highest performance was obtained using a Mamba-based encoder and a CNN-based decoder. This highlights the need to further explore selective SSM-based components in remote sensing semantic segmentation architectures. When a limited training set is available, our results also suggest that incorporating CNN-based components can improve model performance. Further, DL-generated feature spaces can serve as a means to generate data abstractions for use in traditional ML workflows, suggesting value in further developing hybrid workflows that reduce computational demand for end users. Feature reduction can be implemented to further reduce the computational load without reduction in classification performance.

Acknowledgements

The authors would like to thank X anonymous reviewers whose comments strengthened the work. We would also like to thank the developers of the Mamba-UNet and Swin-UNet algorithms and the LandCover.ai dataset.

Data availability

The Landcover.ai (Version 1) dataset used in this study is available for download at the following website: https://landcover.ai.linuxpolska.com/.

References

1. Hassaballah M, Awad AI. Deep learning in computer vision: principles and applications. CRC Press; 2020.

2. Hoeser T, Bachofer F, Kuenzer C. Object Detection and Image Segmentation with Deep Learning on Earth Observation Data: A Review—Part II: Applications. Remote Sens. 2020;12: 3053. doi:10.3390/rs12183053

3. Hoeser T, Kuenzer C. Object Detection and Image Segmentation with Deep Learning on Earth Observation Data: A Review-Part I: Evolution and Recent Trends. Remote Sens. 2020;12: 1667. doi:10.3390/rs12101667

4. Maxwell AE, Ramezan CA, He Y. Chapter 12 - Deep learning for pixel-level predictions. In: Maxwell AE, Ramezan CA, He Y, editors. Supervised Learning in Remote Sensing and Geospatial Science. Elsevier; 2026. pp. 293–315. doi:https://doi.org/10.1016/B978-0-443-29306-1.00011-9

5. Zhang A, Lipton ZC, Li M, Smola AJ. Dive into Deep Learning. Cambridge University Press; 2023.

6. Breiman L. Random forests. Mach Learn. 2001;45: 5–32.

7. Cortes C, Vapnik V. Support-vector networks. Mach Learn. 1995;20: 273–297.

8. Hall-Beyer M. Practical guidelines for choosing GLCM textures to use in landscape classification tasks over a range of moderate spatial scales. Int J Remote Sens. 2017;38: 1312–1338.

9. Haralick RM, Shanmugam K, Dinstein IH. Textural features for image classification. IEEE Trans Syst Man Cybern. 1973; 610–621.

10. Warner T. Kernel-based texture in remote sensing image classification. Geogr Compass. 2011;5: 781–798.

11. Blaschke T. Object based image analysis for remote sensing. ISPRS J Photogramm Remote Sens. 2010;65: 2–16. doi:10.1016/j.isprsjprs.2009.06.004

12. Chen G, Weng Q, Hay GJ, He Y. Geographic object-based image analysis (GEOBIA): emerging trends and future opportunities. GIScience Remote Sens. 2018;55: 159–182. doi:10.1080/15481603.2018.1426092

13. Hay GJ, Blaschke T. Geographic object-based image analysis (GEOBIA). Photogramm Eng Remote Sens. 2010;76: 121.

14. LeCun Y, Bengio Y, Hinton G. Deep learning. nature. 2015;521: 436–444.

15. LeCun Y, Bengio Y, others. Convolutional networks for images, speech, and time series. Handb Brain Theory Neural Netw. 1995;3361: 1995.

16. Dosovitskiy A. An image is worth 16x16 words: Transformers for image recognition at scale. ArXiv Prepr ArXiv201011929. 2020.

17. Vaswani A, Shazeer N, Parmar N, Uszkoreit J, Jones L, Gomez AN, et al. Attention is all you need. Adv Neural Inf Process Syst. 2017;30.

18. Gu A, Dao T. Mamba: Linear-time sequence modeling with selective state spaces. First conference on language modeling. 2024.

19. Liu X, Zhang C, Huang F, Xia S, Wang G, Zhang L. Vision mamba: A comprehensive survey and taxonomy. IEEE Trans Neural Netw Learn Syst. 2025.

20. Liu Y, Tian Y, Zhao Y, Yu H, Xie L, Wang Y, et al. Vmamba: Visual state space model. Adv Neural Inf Process Syst. 2024;37: 103031–103063.

21. Long J, Shelhamer E, Darrell T. Fully convolutional networks for semantic segmentation. Proceedings of the IEEE conference on computer vision and pattern recognition. 2015. pp. 3431–3440.

22. Ronneberger O, Fischer P, Brox T. U-net: Convolutional networks for biomedical image segmentation. Medical Image Computing and Computer-Assisted Intervention–MICCAI 2015: 18th International Conference, Munich, Germany, October 5-9, 2015, Proceedings, Part III 18. Springer; 2015. pp. 234–241.

23. Chen L-C, Papandreou G, Schroff F, Adam H. Rethinking atrous convolution for semantic image segmentation. ArXiv Prepr ArXiv170605587. 2017.

24. Chen L-C, Zhu Y, Papandreou G, Schroff F, Adam H. Encoder-decoder with atrous separable convolution for semantic image segmentation. Proceedings of the European conference on computer vision (ECCV). 2018. pp. 801–818.

25. Zhou Z, Siddiquee MMR, Tajbakhsh N, Liang J. Unet++: Redesigning skip connections to exploit multiscale features in image segmentation. IEEE Trans Med Imaging. 2019;39: 1856–1867.

26. Sun K, Xiao B, Liu D, Wang J. Deep high-resolution representation learning for human pose estimation. Proceedings of the IEEE/CVF conference on computer vision and pattern recognition. 2019. pp. 5693–5703.

27. Huang H, Lin L, Tong R, Hu H, Zhang Q, Iwamoto Y, et al. Unet 3+: A full-scale connected unet for medical image segmentation. ICASSP 2020-2020 IEEE international conference on acoustics, speech and signal processing (ICASSP). IEEE; 2020. pp. 1055–1059.

28. Strudel R, Garcia R, Laptev I, Schmid C. Segmenter: Transformer for Semantic Segmentation. 2021 IEEE/CVF International Conference on Computer Vision (ICCV). Montreal, QC, Canada: IEEE; 2021. pp. 7242–7252. doi:10.1109/ICCV48922.2021.00717

29. Xie E, Wang W, Yu Z, Anandkumar A, Alvarez JM, Luo P. SegFormer: Simple and efficient design for semantic segmentation with transformers. Adv Neural Inf Process Syst. 2021;34: 12077–12090.

30. Chu X, Tian Z, Wang Y, Zhang B, Ren H, Wei X, et al. Twins: Revisiting the design of spatial attention in vision transformers. Adv Neural Inf Process Syst. 2021;34: 9355–9366.

31. Cao H, Wang Y, Chen J, Jiang D, Zhang X, Tian Q, et al. Swin-unet: Unet-like pure transformer for medical image segmentation. European conference on computer vision. Springer; 2022. pp. 205–218.

32. Chen J, Lu Y, Yu Q, Luo X, Adeli E, Wang Y, et al. Transunet: Transformers make strong encoders for medical image segmentation. ArXiv Prepr ArXiv210204306. 2021.

33. Hatamizadeh A, Tang Y, Nath V, Yang D, Myronenko A, Landman B, et al. Unetr: Transformers for 3d medical image segmentation. Proceedings of the IEEE/CVF winter conference on applications of computer vision. 2022. pp. 574–584.

34. Wang Z, Zheng J-Q, Zhang Y, Cui G, Li L. Mamba-unet: Unet-like pure visual mamba for medical image segmentation. ArXiv Prepr ArXiv240205079. 2024.

35. Ma J, Li F, Wang B. U-mamba: Enhancing long-range dependency for biomedical image segmentation. ArXiv Prepr ArXiv240104722. 2024.

36. Ruan J, Li J, Xiang S. Vm-unet: Vision mamba unet for medical image segmentation. ACM Trans Multimed Comput Commun Appl. 2024.

37. Ma X, Zhang X, Pun M-O. Rs 3 mamba: Visual state space model for remote sensing image semantic segmentation. IEEE Geosci Remote Sens Lett. 2024;21: 1–5.

38. Cortes C, Mohri M, Rostamizadeh A. Algorithms for learning kernels based on centered alignment. J Mach Learn Res. 2012;13: 795–828.

39. Gretton A, Bousquet O, Smola A, Schölkopf B. Measuring statistical dependence with Hilbert-Schmidt norms. International conference on algorithmic learning theory. Springer; 2005. pp. 63–77.

40. Kornblith S, Norouzi M, Lee H, Hinton G. Similarity of neural network representations revisited. International conference on machine learning. PMlR; 2019. pp. 3519–3529.

41. Mantel N. The Detection of Disease Clustering and a Generalized Regression Approach. Cancer Res. 1967;27: 209–220.

42. Jolliffe I. Principal component analysis. International encyclopedia of statistical science. Springer; 2011. pp. 1094–1096.

43. Schölkopf B, Smola A, Müller K-R. Nonlinear component analysis as a kernel eigenvalue problem. Neural Comput. 1998;10: 1299–1319.

44. Hyvärinen A, Hurri J, Hoyer PO. Independent component analysis. Natural Image Statistics: A Probabilistic Approach to Early Computational Vision. Springer; 2001. pp. 151–175.

45. Debeer D, Strobl C. Conditional permutation importance revisited. BMC Bioinformatics. 2020;21: 1–30.

46. He K, Zhang X, Ren S, Sun J. Deep Residual Learning for Image Recognition. ArXiv151203385 Cs. 2015 [cited 2 Jan 2021]. Available: http://arxiv.org/abs/1512.03385

47. Ioffe S, Szegedy C. Batch normalization: Accelerating deep network training by reducing internal covariate shift. International conference on machine learning. PMLR; 2015. pp. 448–456.

48. Luo P, Wang X, Shao W, Peng Z. Towards understanding regularization in batch normalization. ArXiv Prepr ArXiv180900846. 2018.

49. Santurkar S, Tsipras D, Ilyas A, Madry A. How does batch normalization help optimization? Adv Neural Inf Process Syst. 2018;31.

50. Nwankpa C, Ijomah W, Gachagan A, Marshall S. Activation functions: Comparison of trends in practice and research for deep learning. ArXiv Prepr ArXiv181103378. 2018.

51. Sharma S, Sharma S, Athaiya A. Activation functions in neural networks. Data Sci. 2017;6: 310–316.

52. Liu Z, Lin Y, Cao Y, Hu H, Wei Y, Zhang Z, et al. Swin transformer: Hierarchical vision transformer using shifted windows. Proceedings of the IEEE/CVF international conference on computer vision. 2021. pp. 10012–10022.

53. Boguszewski A, Batorski D, Ziemba-Jankowska N, Dziedzic T, Zambrzycka A. LandCover. ai: Dataset for automatic mapping of buildings, woodlands, water and roads from aerial imagery. Proceedings of the IEEE/CVF conference on computer vision and pattern recognition. 2021. pp. 1102–1110.

54. Welcome to Python.org. In: Python.org [Internet]. [cited 17 Oct 2022]. Available: https://www.python.org/

55. PyTorch. [cited 30 Oct 2023]. Available: https://pytorch.org/

56. CUDA Toolkit - Free Tools and Training. In: NVIDIA Developer [Internet]. [cited 30 Oct 2023]. Available: https://developer.nvidia.com/cuda-toolkit

57. CUDA Deep Neural Network (cuDNN) | NVIDIA Developer. [cited 30 Oct 2023]. Available: https://developer.nvidia.com/cudnn

58. Iakubovskii P. Segmentation Models Pytorch. GitHub repository. GitHub; 2019. Available: https://github.com/qubvel/segmentation_models.pytorch

59. Deng J, Dong W, Socher R, Li L-J, Li K, Fei-Fei L. Imagenet: A large-scale hierarchical image database. 2009 IEEE conference on computer vision and pattern recognition. Ieee; 2009. pp. 248–255.

60. Oksanen J, Simpson GL, Blanchet FG, Kindt R, Legendre P, Minchin PR, et al. vegan: Community Ecology Package. 2026. Available: https://vegandevs.github.io/vegan/

61. Kuhn M, Wickham H. Tidymodels: a collection of packages for modeling and machine learning using tidyverse principles. 2020. Available: https://www.tidymodels.org

62. R Core Team. R: A Language and Environment for Statistical Computing. Vienna, Austria: R Foundation for Statistical Computing; 2025. Available: https://www.R-project.org/

63. Wright MN, Ziegler A. ranger: A Fast Implementation of Random Forests for High Dimensional Data in C++ and R. J Stat Softw. 2017;77: 1–17. doi:10.18637/jss.v077.i01

64. Karatzoglou A, Smola A, Hornik K, Zeileis A. kernlab – An S4 Package for Kernel Methods in R. J Stat Softw. 2004;11: 1–20. doi:10.18637/jss.v011.i09

65. Kuhn M, Wickham H, Hvitfeldt E. recipes: Preprocessing and Feature Engineering Steps for Modeling. 2024. Available: https://CRAN.R-project.org/package=recipes

66. Maxwell A, Farhadpour S. micer: Map Image Classification Efficacy. 2025. Available: https://CRAN.R-project.org/package=micer

67. Maxwell AE, Ramezan CA, He Y. Chapter 5 - Model assessment methods and metrics. In: Maxwell AE, Ramezan CA, He Y, editors. Supervised Learning in Remote Sensing and Geospatial Science. Elsevier; 2026. pp. 103–135. doi:https://doi.org/10.1016/B978-0-443-29306-1.00005-3

68. Shao G, Tang L, Zhang H. Introducing image classification efficacies. IEEE Access. 2021;9: 134809–134816.

69. Tang L, Shao J, Pang S, Wang Y, Maxwell A, Hu X, et al. Bolstering performance evaluation of image segmentation models with efficacy metrics in the absence of a gold standard. IEEE Trans Geosci Remote Sens. 2024.

70. Gregorutti B, Michel B, Saint-Pierre P. Correlation and variable importance in random forests. Stat Comput. 2017;27: 659–678.

71. Maxwell AE, Ramezan CA, He Y. Chapter 4 - Data preparation and preprocessing. In: Maxwell AE, Ramezan CA, He Y, editors. Supervised Learning in Remote Sensing and Geospatial Science. Elsevier; 2026. pp. 69–101. doi:https://doi.org/10.1016/B978-0-443-29306-1.00001-6

72. Strobl C, Boulesteix A-L, Kneib T, Augustin T, Zeileis A. Conditional variable importance for random forests. BMC Bioinformatics. 2008;9: 307.

73. Strobl C, Boulesteix A-L, Zeileis A, Hothorn T. Bias in random forest variable importance measures: Illustrations, sources and a solution. BMC Bioinformatics. 2007;8: 25.

74. Debeer D, Hothorn T, Strobl C. permimp: Conditional Permutation Importance. 2021. Available: https://CRAN.R-project.org/package=permimp

75. Raghu M, Unterthiner T, Kornblith S, Zhang C, Dosovitskiy A. Do vision transformers see like convolutional neural networks? Adv Neural Inf Process Syst. 2021;34: 12116–12128.

76. Smith SL, Brock A, Berrada L, De S. Convnets match vision transformers at scale. ArXiv Prepr ArXiv231016764. 2023.

77. Yuan L, Chen Y, Wang T, Yu W, Shi Y, Jiang Z-H, et al. Tokens-to-token vit: Training vision transformers from scratch on imagenet. Proceedings of the IEEE/CVF international conference on computer vision. 2021. pp. 558–567.

78. Zhai X, Kolesnikov A, Houlsby N, Beyer L. Scaling vision transformers. Proceedings of the IEEE/CVF conference on computer vision and pattern recognition. 2022. pp. 12104–12113.

79. Liu M, Dan J, Lu Z, Yu Y, Li Y, Li X. CM-UNet: Hybrid CNN-Mamba UNet for remote sensing image semantic segmentation. ArXiv Prepr ArXiv240510530. 2024.

80. Dietterich TG. Ensemble methods in machine learning. International workshop on multiple classifier systems. Springer; 2000. pp. 1–15.

81. Brown CF, Kazmierski MR, Pasquarella VJ, Rucklidge WJ, Samsikova M, Zhang C, et al. Alphaearth foundations: An embedding field model for accurate and efficient global mapping from sparse label data. ArXiv Prepr ArXiv250722291. 2025.

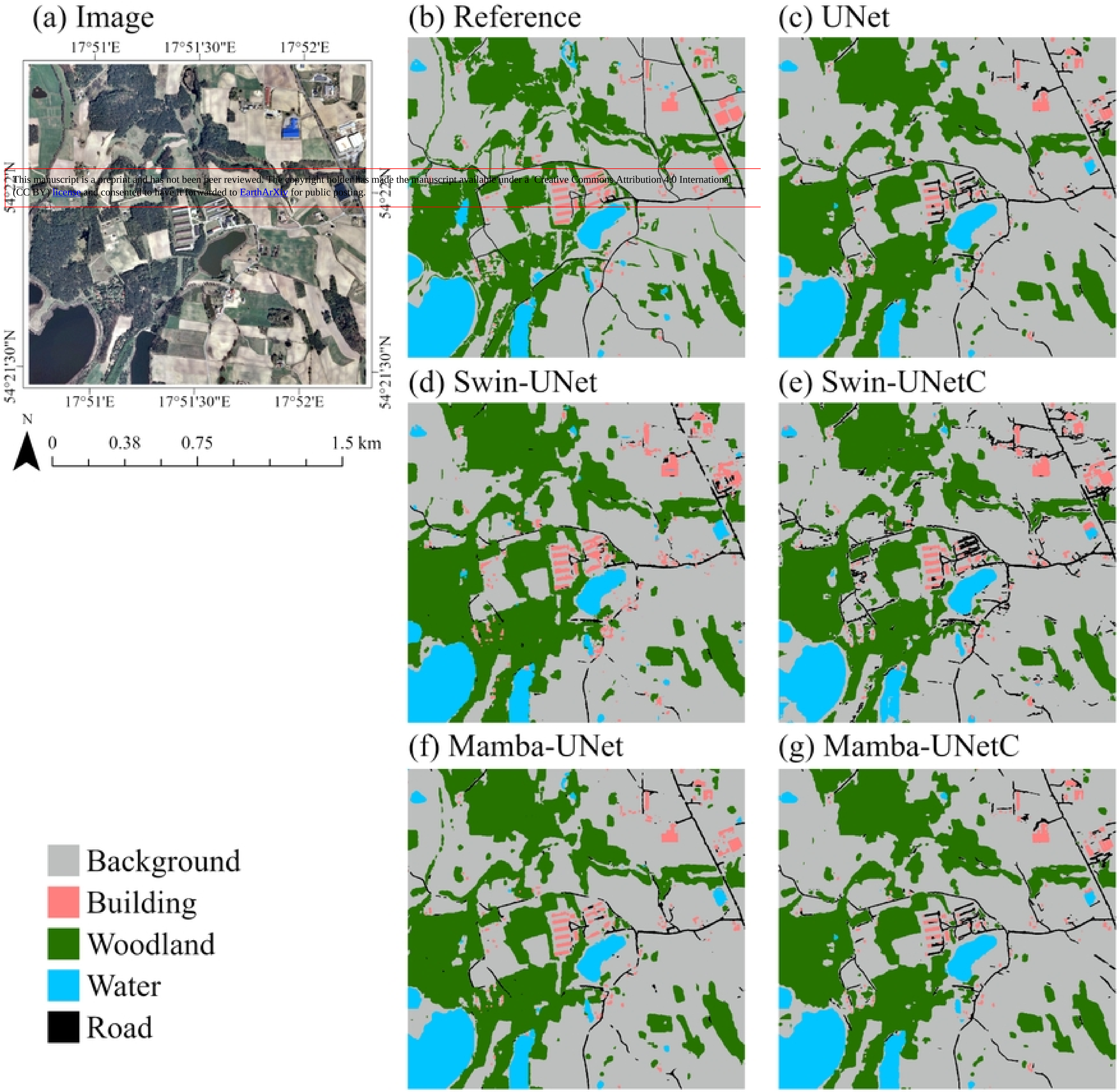
(a) Image
17°51'E
17°51'30"E
17°52'E
54°21'30"N
N
0
0.38
0.75
1.5 km
(b) Reference
(c) UNet
(d) Swin-UNet
(e) Swin-UNetC
(f) Mamba-UNet
(g) Mamba-UNetC
Background
Building
Woodland
Water
Road

Figure 5

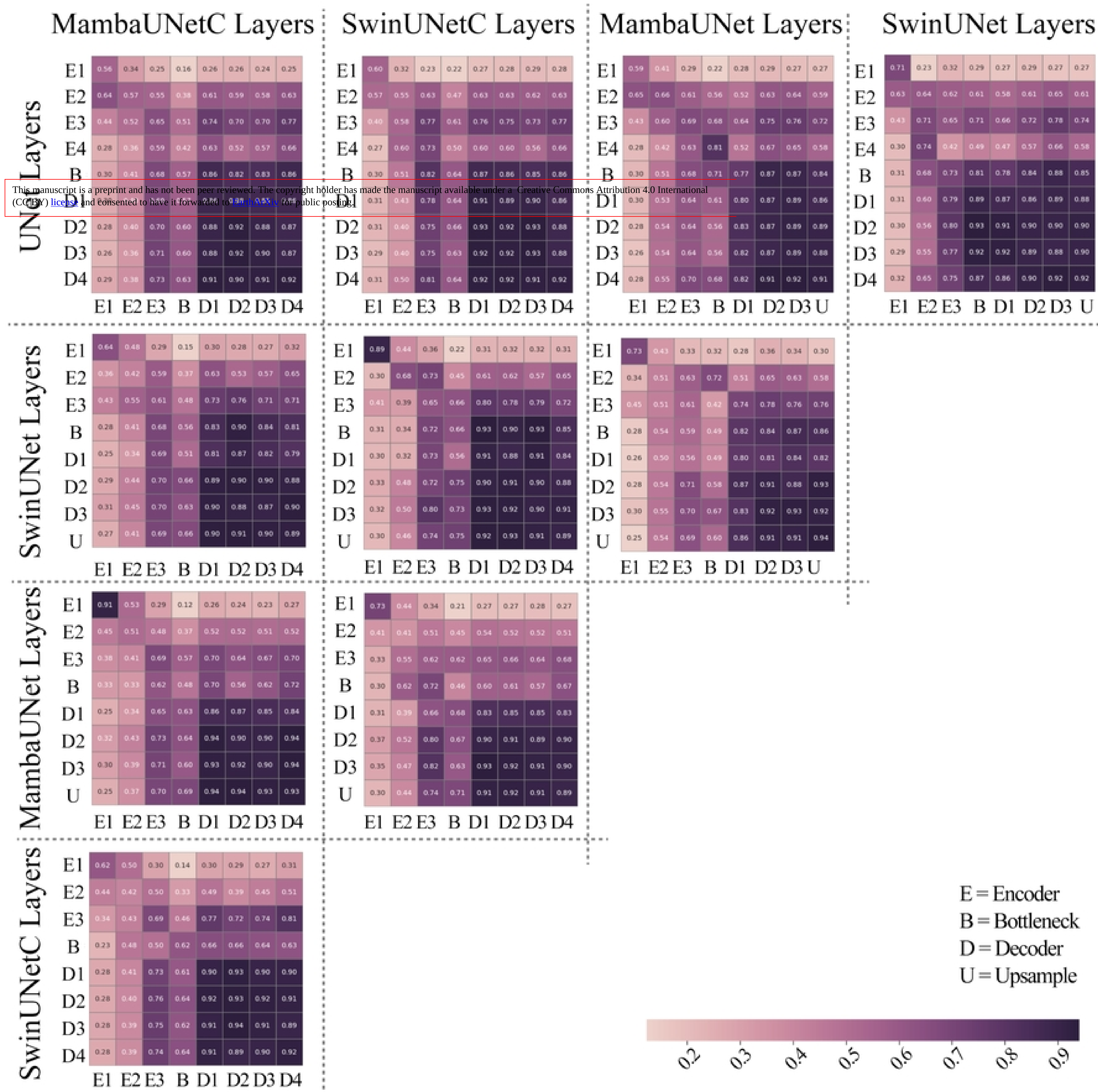

MambaUNetC Layers
SwinUNetC Layers
MambaUNet Layers
SwinUNet Layers
UNet Layers
SwinUNet Layers
MambaUNet Layers
SwinUNetC Layers
E1 E2 E3 E4 B D1 D2 D3 D4
E1 E2 E3 B D1 D2 D3 D4
E1 E2 E3 B D1 D2 D3 U
E = Encoder
B = Bottleneck
D = Decoder
U = Upsample
0.2 0.3 0.4 0.5 0.6 0.7 0.8 0.9

Figure 6

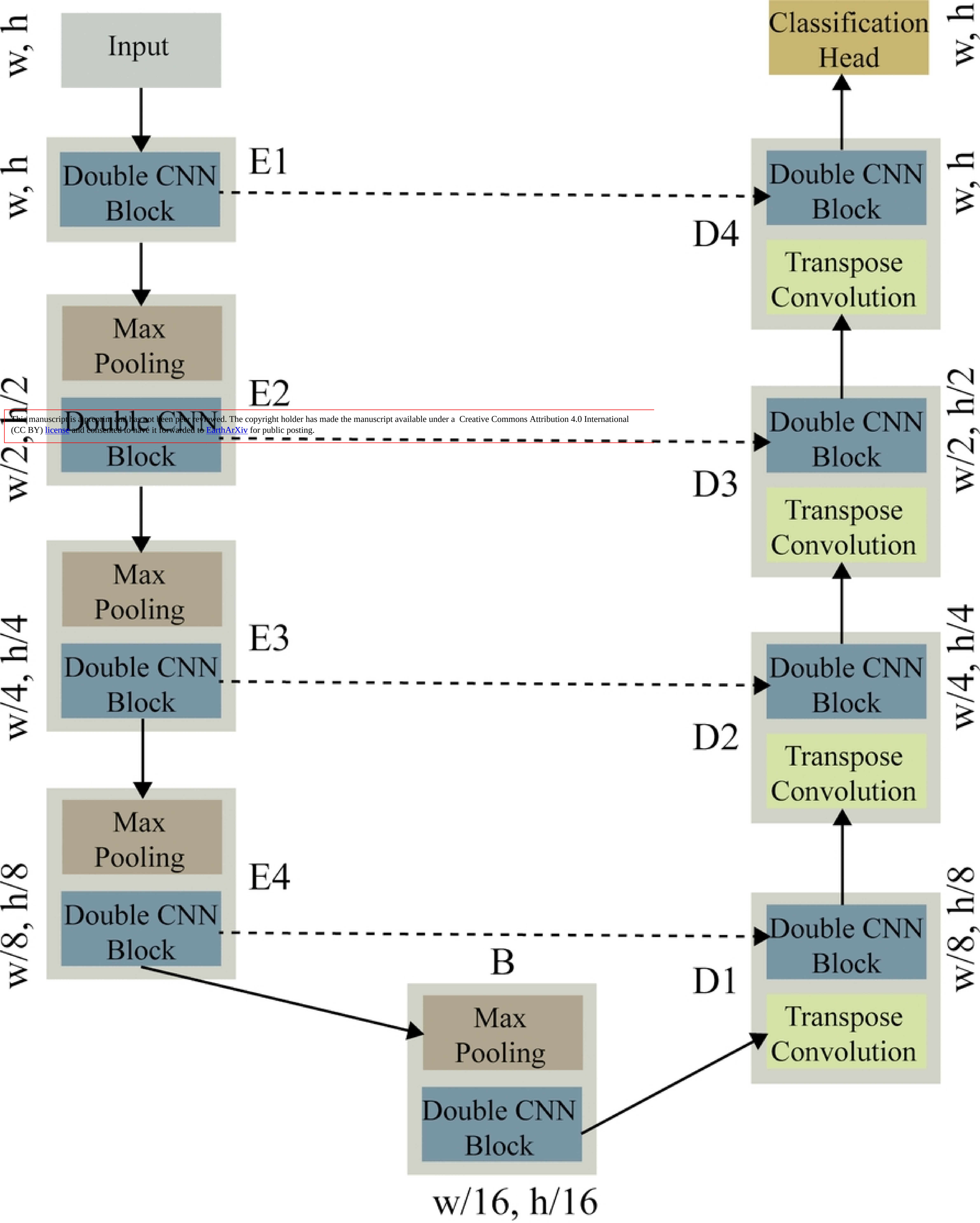
Input
Double CNN Block
Max Pooling
Classification Head
Transpose Convolution
E1
E2
E3
E4
B
D1
D2
D3
D4
w, h
w/2, h/2
w/4, h/4
w/8, h/8
w/16, h/16

Figure 1

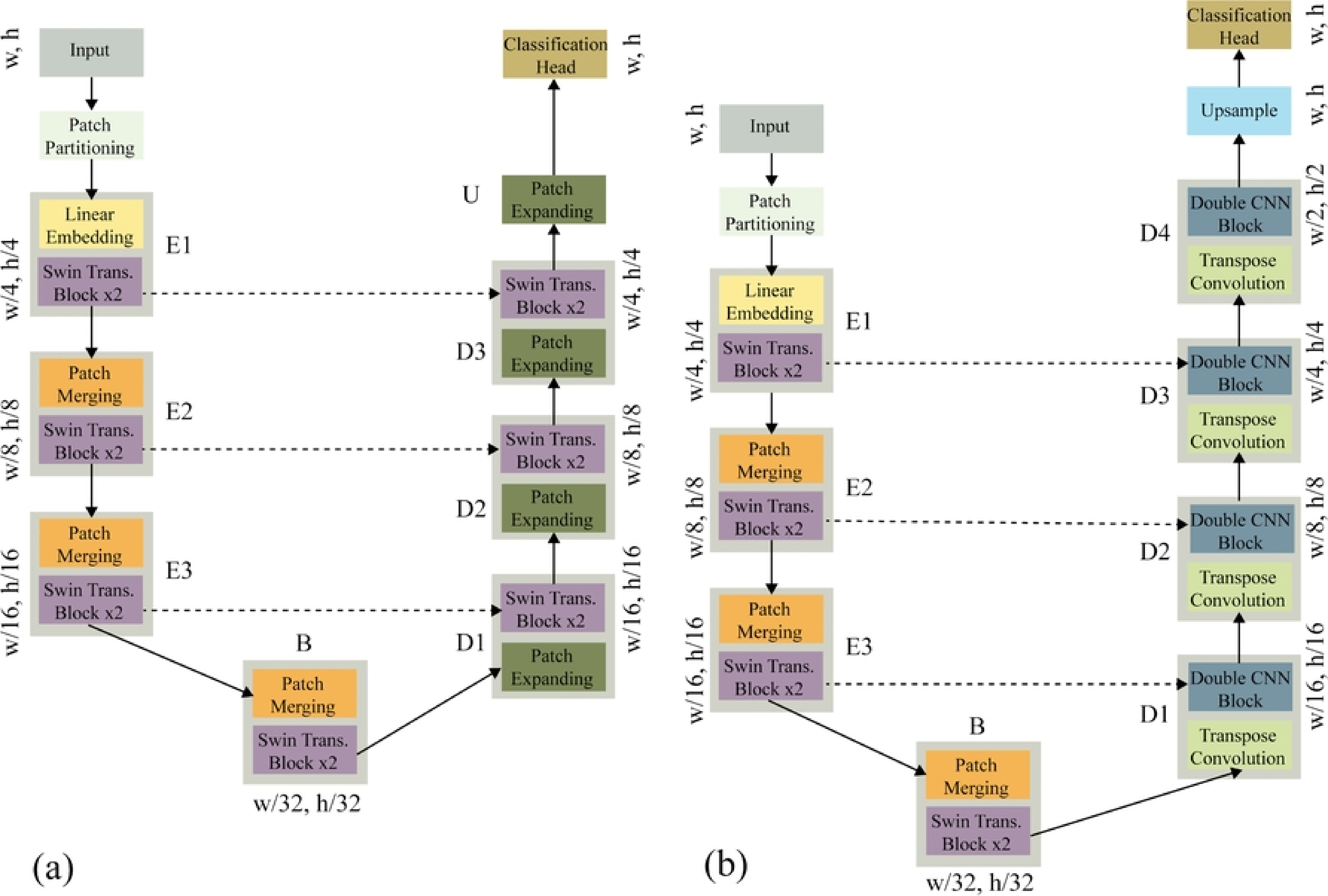

w, h
Input
Patch Partitioning
w/4, h/4
Linear Embedding
Swin Trans. Block x2
E1
w/8, h/8
Patch Merging
Swin Trans. Block x2
E2
w/16, h/16
Patch Merging
Swin Trans. Block x2
E3
B
Patch Merging
Swin Trans. Block x2
w/32, h/32
D1
Patch Expanding
Swin Trans. Block x2
w/16, h/16
D2
Patch Expanding
Swin Trans. Block x2
w/8, h/8
D3
Patch Expanding
Swin Trans. Block x2
w/4, h/4
U
Patch Expanding
Classification Head
w, h
(a)
w, h
Input
Patch Partitioning
w/4, h/4
Linear Embedding
Swin Trans. Block x2
E1
w/8, h/8
Patch Merging
Swin Trans. Block x2
E2
w/16, h/16
Patch Merging
Swin Trans. Block x2
E3
B
Patch Merging
Swin Trans. Block x2
w/32, h/32
D1
Transpose Convolution
Double CNN Block
w/16, h/16
D2
Transpose Convolution
Double CNN Block
w/8, h/8
D3
Transpose Convolution
Double CNN Block
w/4, h/4
D4
Transpose Convolution
Double CNN Block
w/2, h/2
Upsample
w, h
Classification Head
w, h
(b)

Figure 2

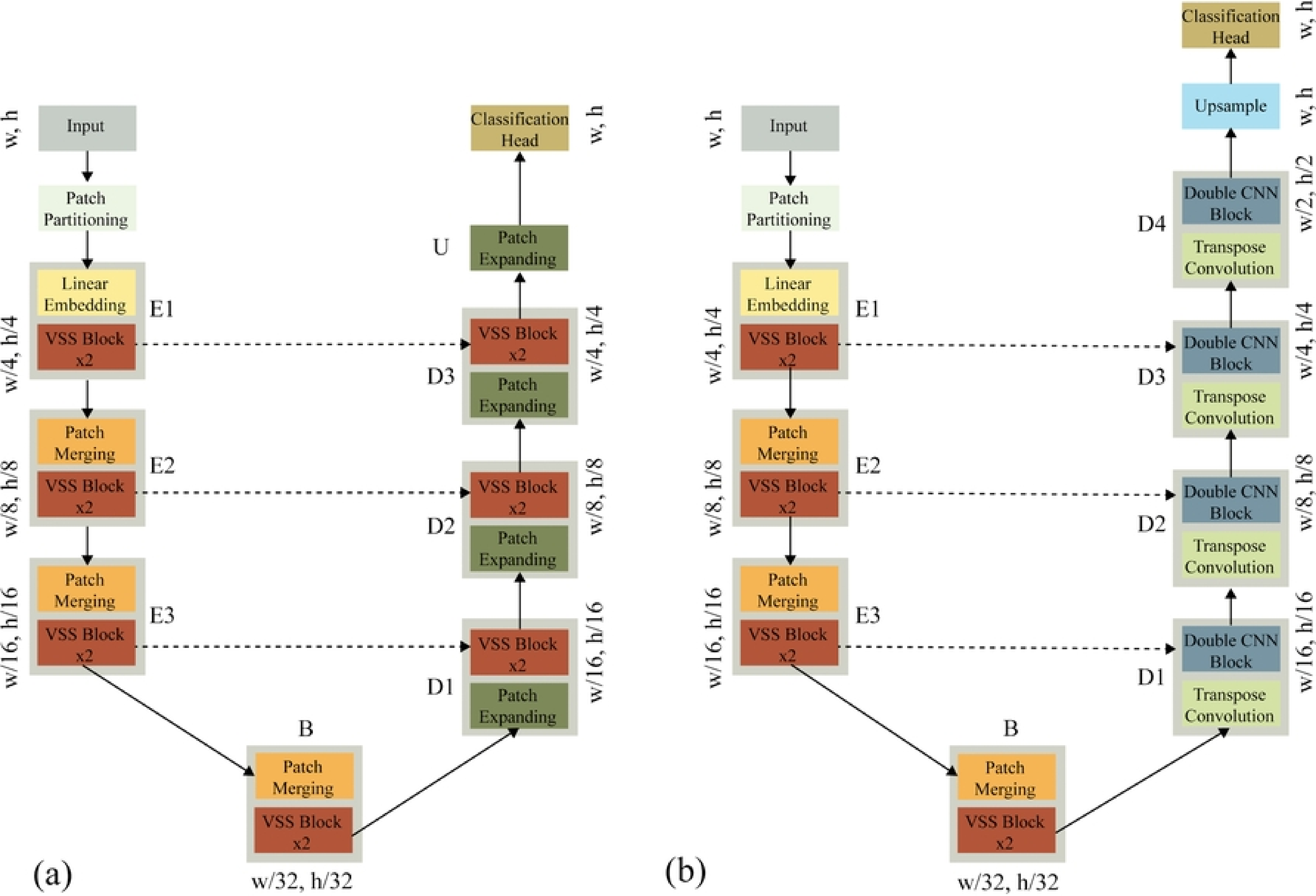

w, h
Input
Patch Partitioning
Linear Embedding
VSS Block x2
E1
w/4, h/4
Patch Merging
VSS Block x2
E2
w/8, h/8
Patch Merging
VSS Block x2
E3
w/16, h/16
B
Patch Merging
VSS Block x2
w/32, h/32
D1
VSS Block x2
Patch Expanding
D2
VSS Block x2
Patch Expanding
D3
VSS Block x2
Patch Expanding
U
Patch Expanding
Classification Head
(a)
Double CNN Block
Transpose Convolution
D4
w/2, h/2
Upsample
(b)

Figure 3

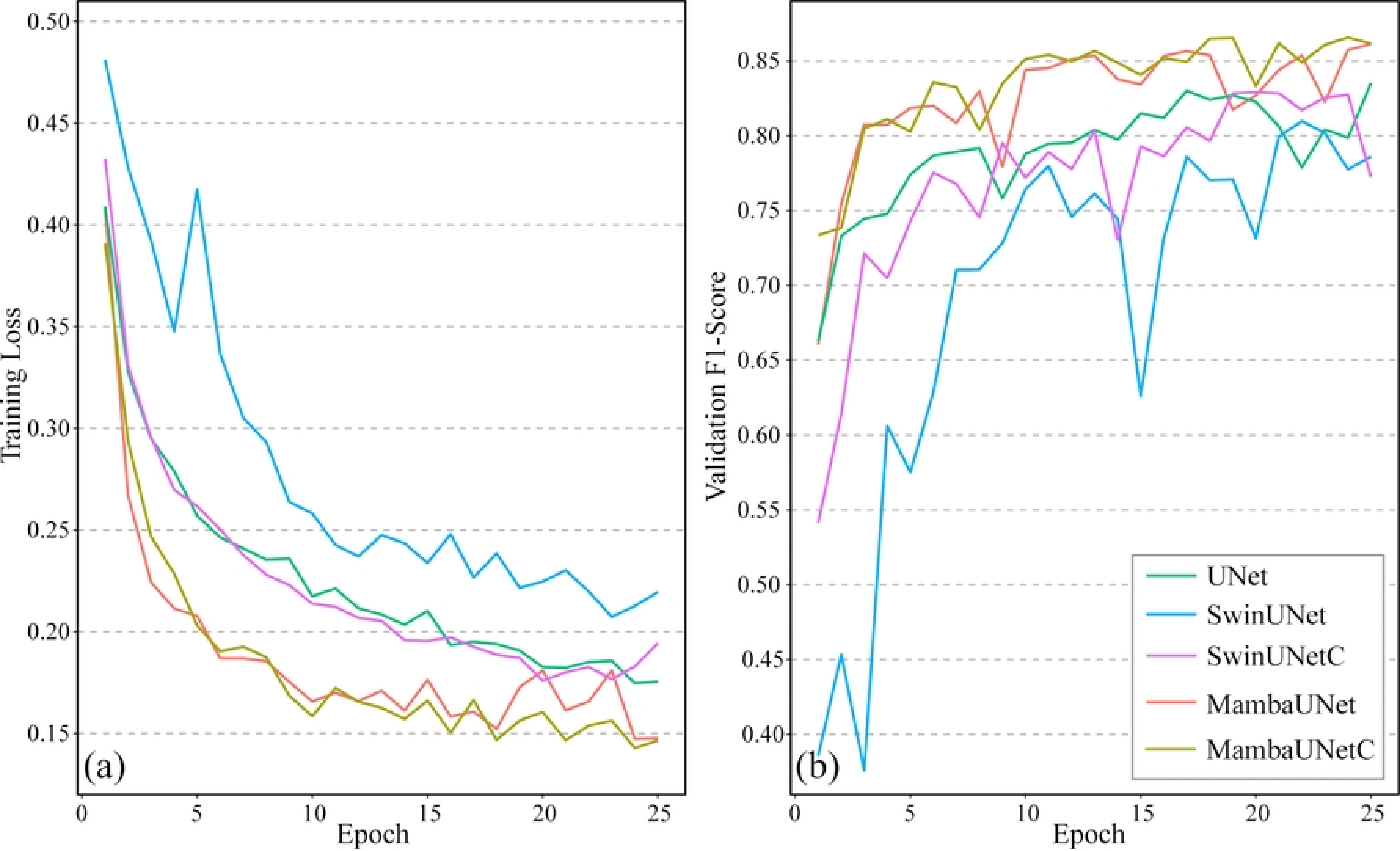
Training Loss
Epoch
(a)
Validation F1-Score
Epoch
(b)
UNet
SwinUNet
SwinUNetC
MambaUNet
MambaUNetC

Figure 4

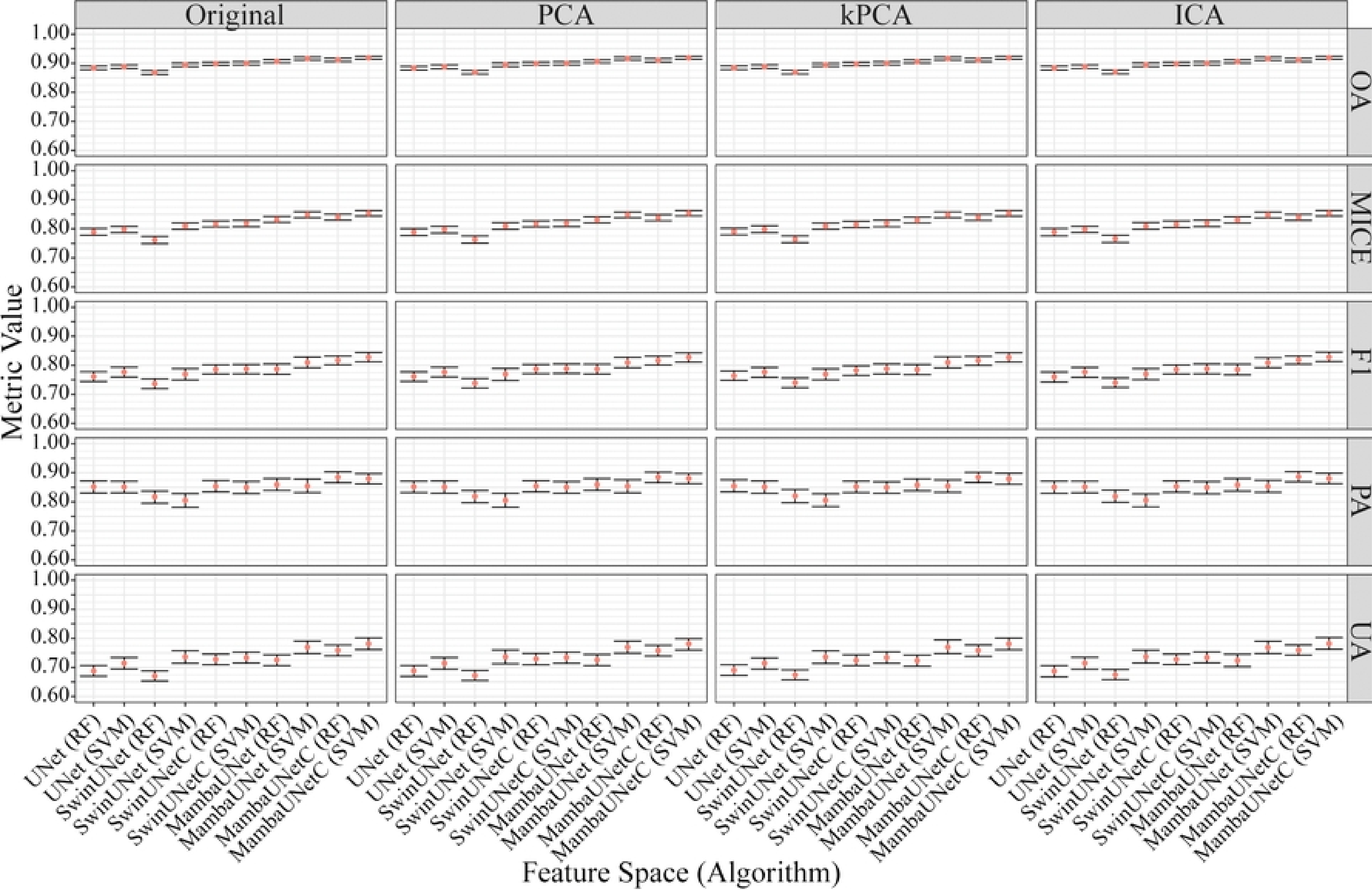
Original
PCA
kPCA
ICA
OA
MICE
F1
PA
UA
Metric Value
1.00
0.90
0.80
0.70
0.60
UNet (RF)
UNet (SVM)
SwinUNet (RF)
SwinUNet (SVM)
SwinUNetC (RF)
SwinUNetC (SVM)
MambaUNet (RF)
MambaUNet (SVM)
MambaUNetC (RF)
MambaUNetC (SVM)
Feature Space (Algorithm)

Figure 7

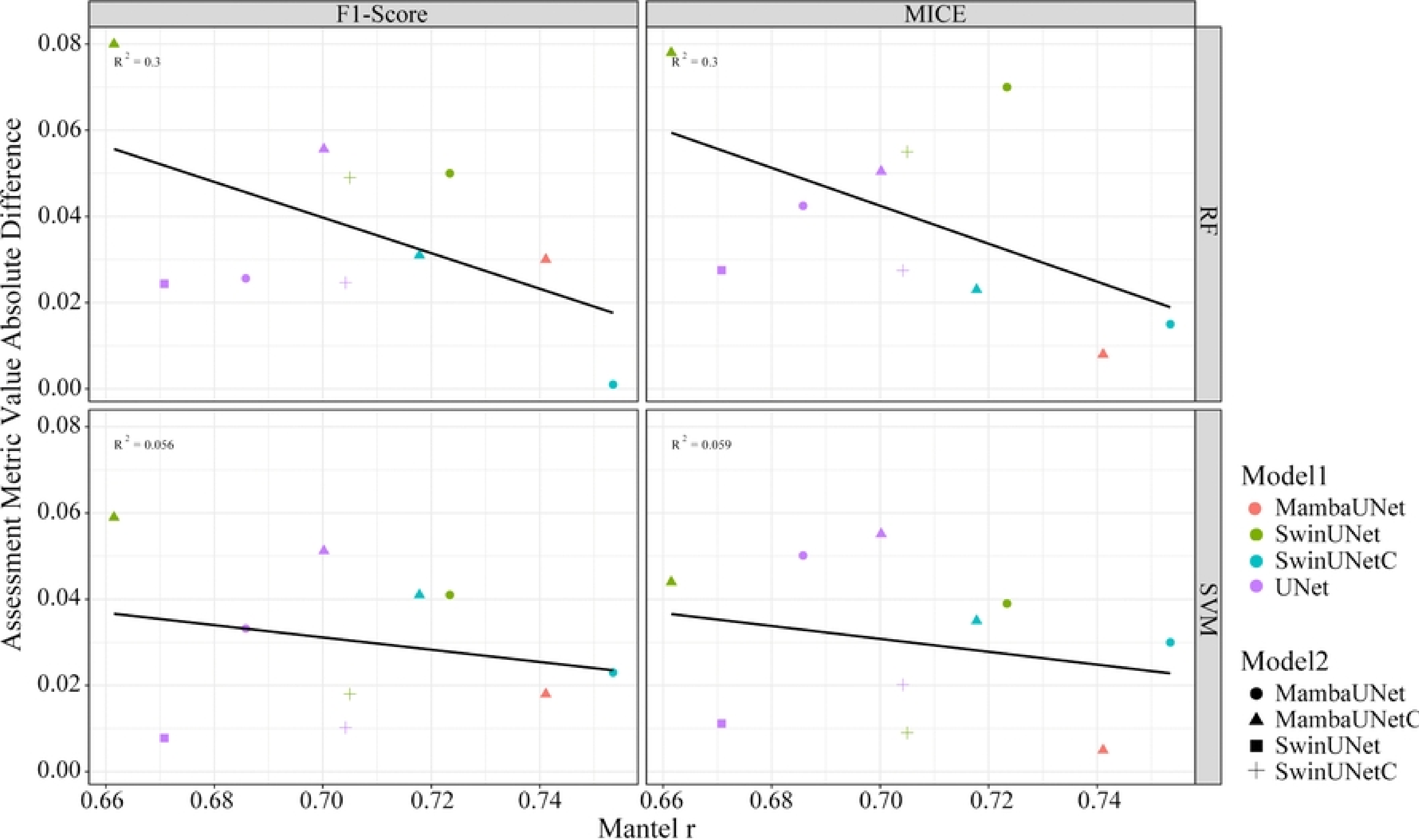
F1-Score
MICE
RF
SVM
$R^2 = 0.3$
$R^2 = 0.3$
$R^2 = 0.056$
$R^2 = 0.059$
Assessment Metric Value Absolute Difference
0.00
0.02
0.04
0.06
0.08
Mantel r
0.66
0.68
0.70
0.72
0.74
Model1
MambaUNet
SwinUNet
SwinUNetC
UNet
Model2
MambaUNet
MambaUNetC
SwinUNet
SwinUNetC

Figure 8

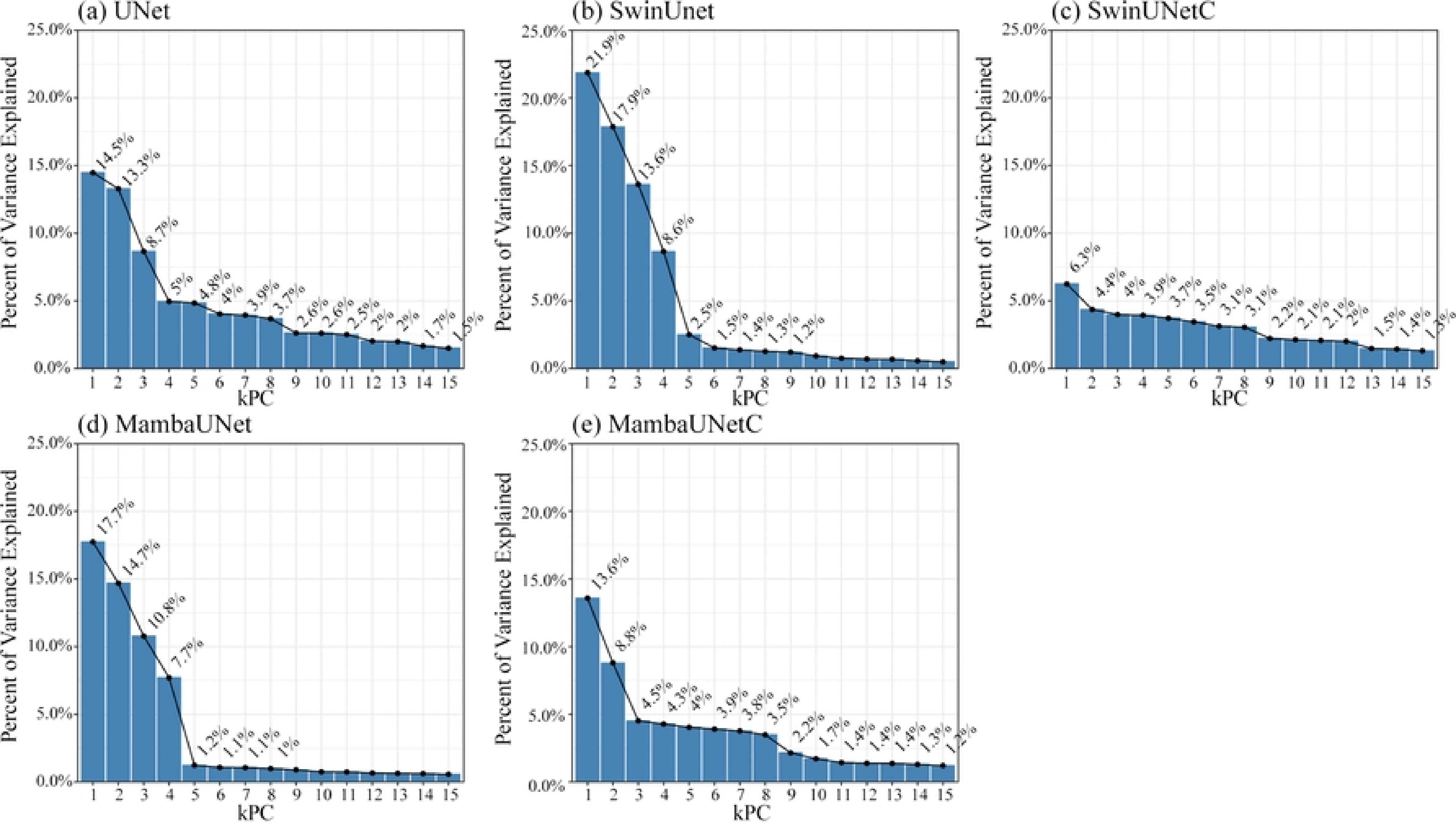
(a) UNet
(b) SwinUnet
(c) SwinUNetC
(d) MambaUNet
(e) MambaUNetC
Percent of Variance Explained
kPC
14.5%
13.3%
8.7%
5%
4.8%
4%
3.9%
3.7%
2.6%
2.6%
2.5%
2%
2%
1.7%
1.5%
21.9%
17.9%
13.6%
8.6%
2.5%
1.5%
1.4%
1.3%
1.2%
6.3%
4.4%
4%
3.9%
3.7%
3.5%
3.1%
3.1%
2.2%
2.1%
2.1%
2%
1.5%
1.4%
1.3%
17.7%
14.7%
10.8%
7.7%
1.2%
1.1%
1.1%
1%
13.6%
8.8%
4.5%
4.3%
4%
3.9%
3.8%
3.5%
2.2%
1.7%
1.4%
1.4%
1.4%
1.3%
1.2%

Figure 9

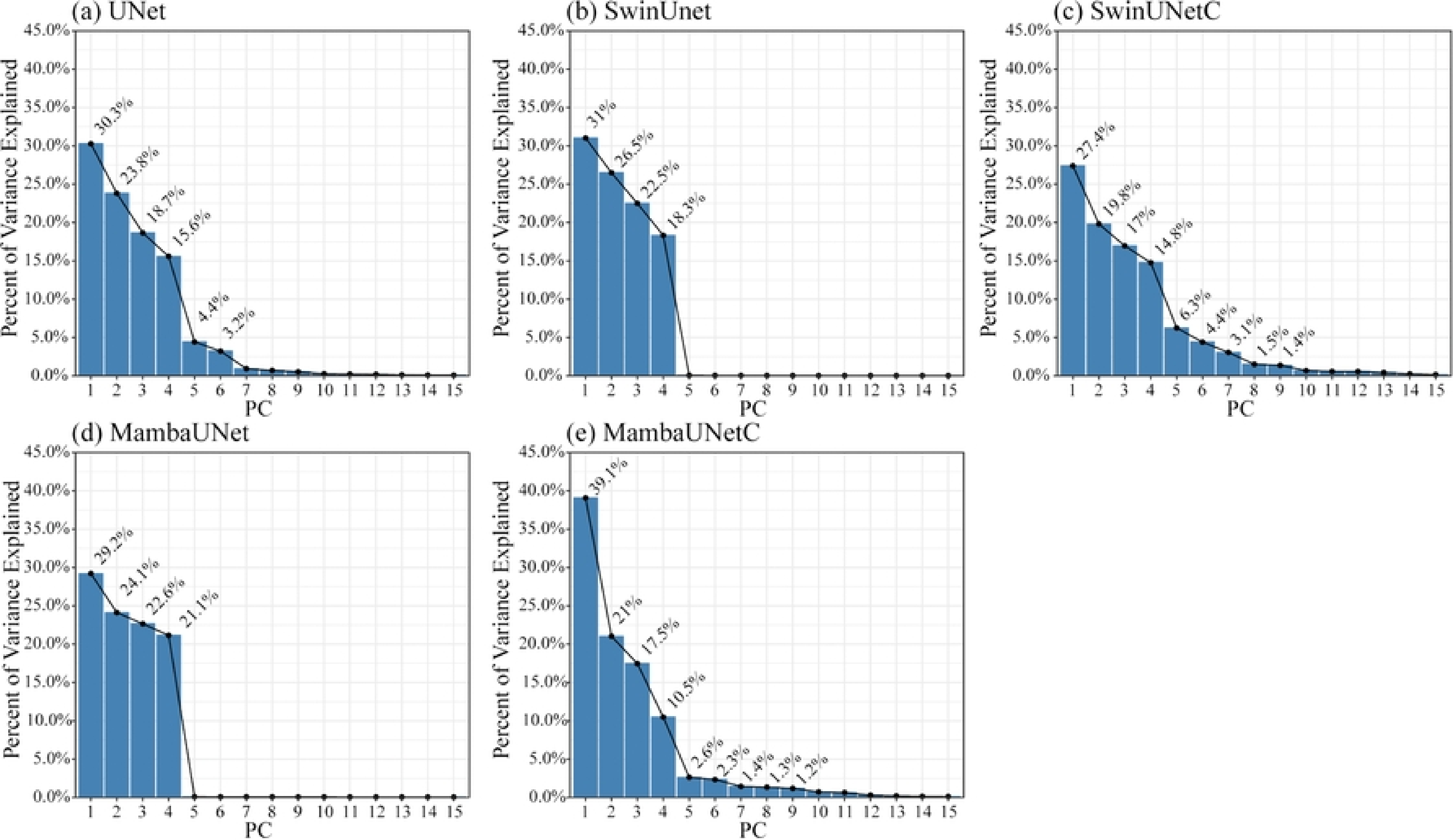
(a) UNet
(b) SwinUnet
(c) SwinUNetC
(d) MambaUNet
(e) MambaUNetC
Percent of Variance Explained
PC
30.3%
23.8%
18.7%
15.6%
4.4%
3.2%
31%
26.5%
22.5%
18.3%
27.4%
19.8%
17%
14.8%
6.3%
4.4%
3.1%
1.5%
1.4%
29.2%
24.1%
22.6%
21.1%
39.1%
21%
17.5%
10.5%
2.6%
2.3%
1.4%
1.3%
1.2%

Figure 10

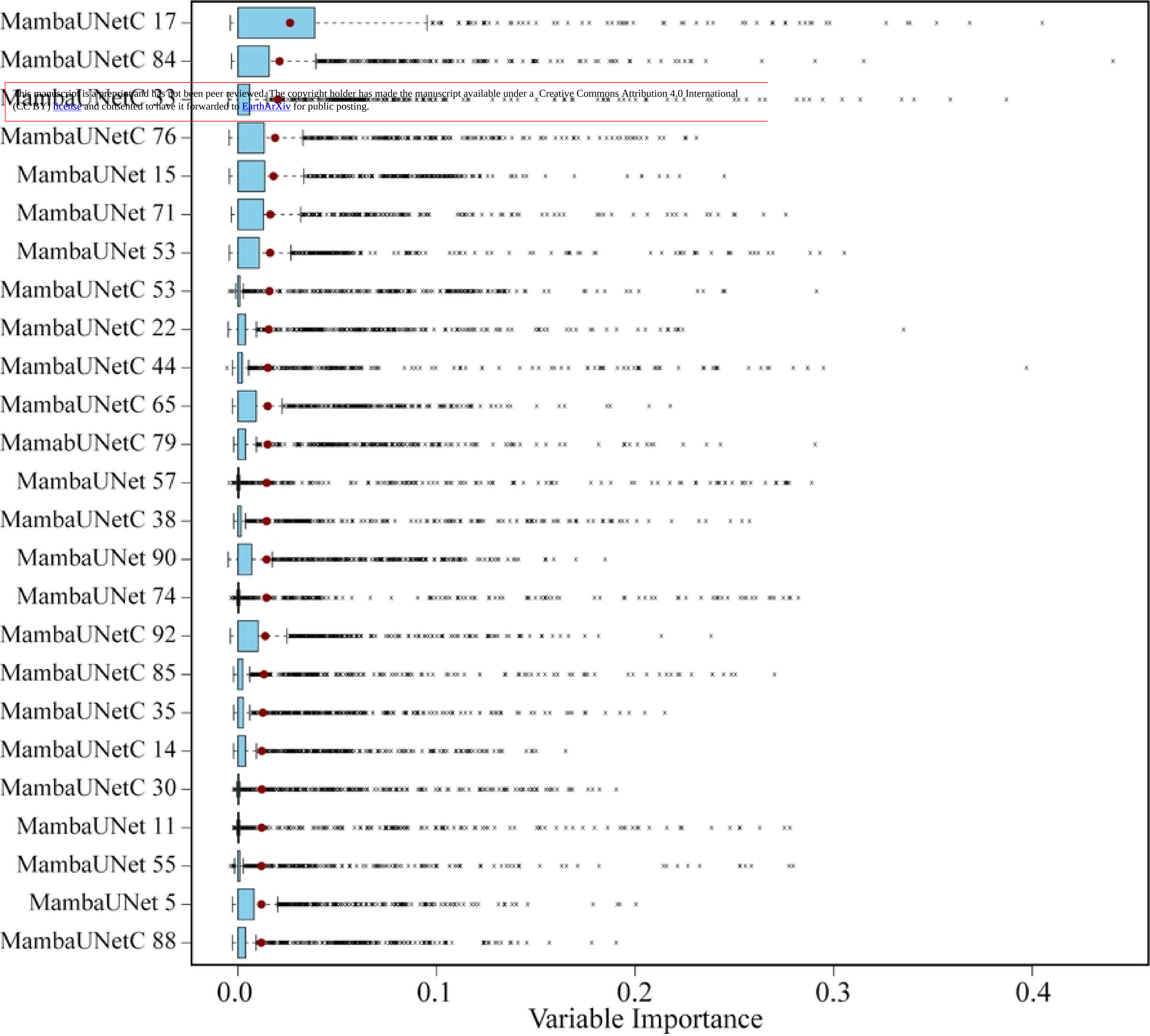
MambaUNetC 17
MambaUNetC 84
MambaUNetC 33
MambaUNetC 76
MambaUNet 15
MambaUNet 71
MambaUNet 53
MambaUNetC 53
MambaUNetC 22
MambaUNetC 44
MambaUNetC 65
MamabUNetC 79
MambaUNet 57
MambaUNetC 38
MambaUNet 90
MambaUNet 74
MambaUNetC 92
MambaUNetC 85
MambaUNetC 35
MambaUNetC 14
MambaUNetC 30
MambaUNet 11
MambaUNet 55
MambaUNet 5
MambaUNetC 88
0.0
0.1
0.2
0.3
0.4
Variable Importance

Figure 11

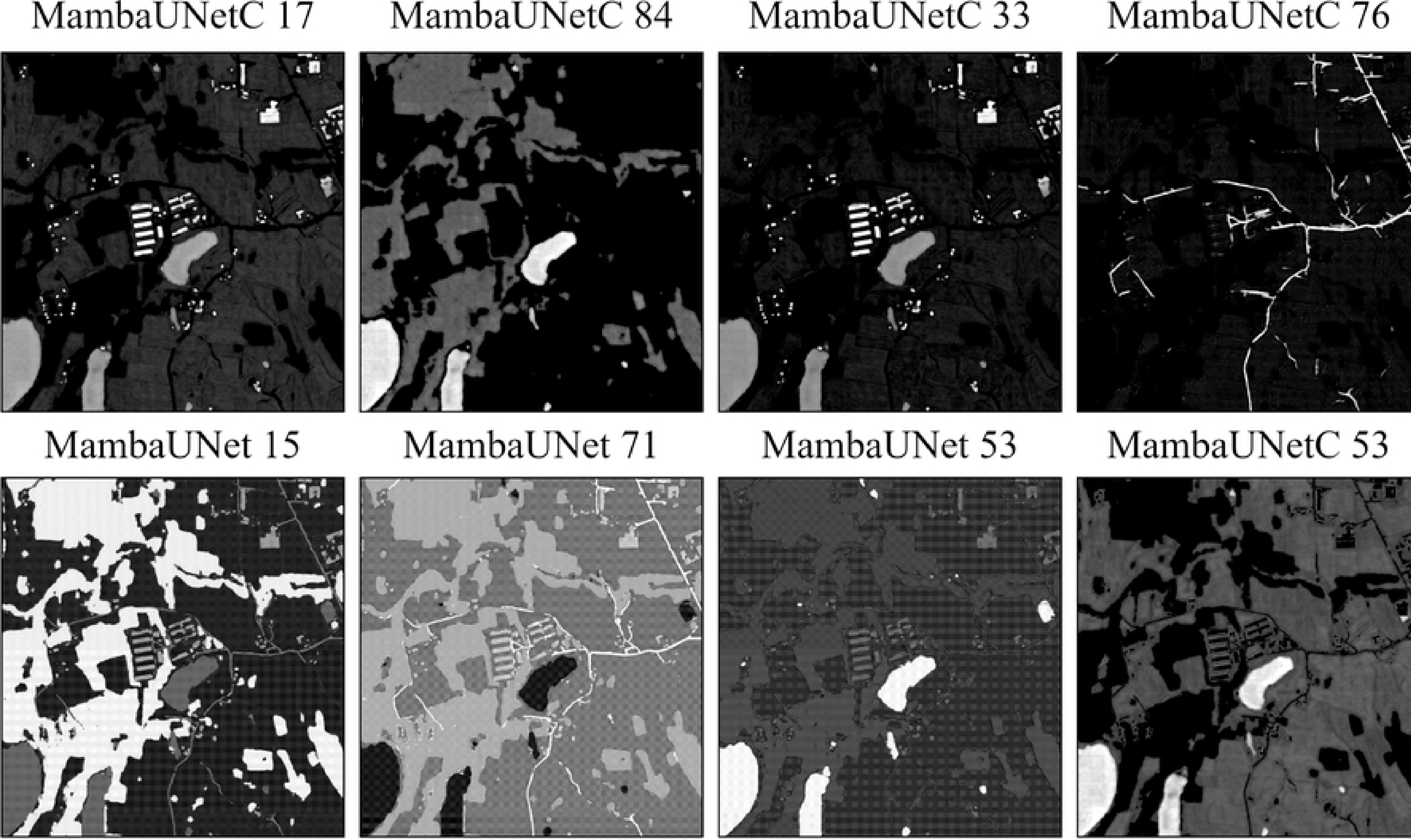
MambaUNetC 17
MambaUNetC 84
MambaUNetC 33
MambaUNetC 76
MambaUNet 15
MambaUNet 71
MambaUNet 53
MambaUNetC 53

Figure 12

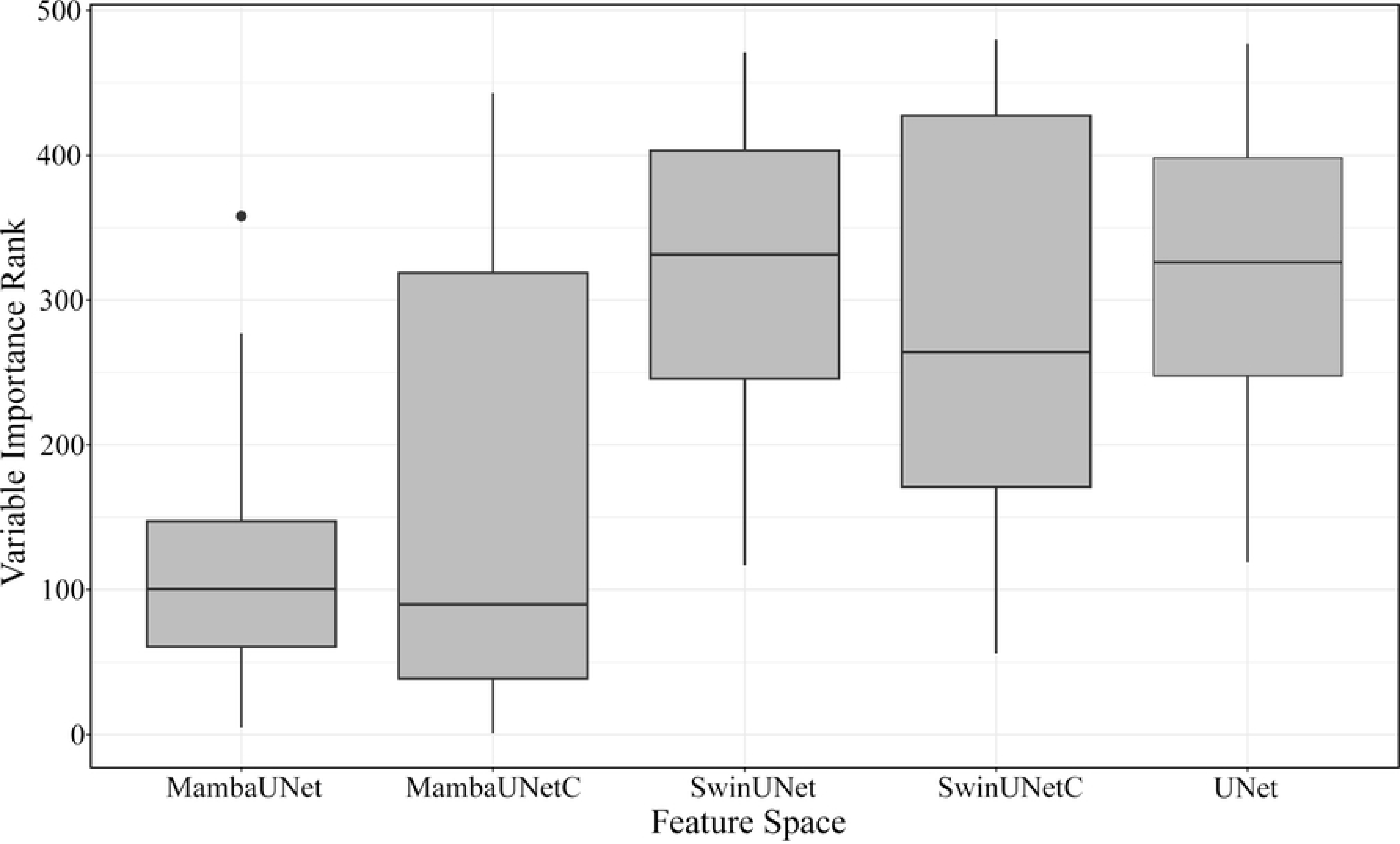
500
400
300
200
100
0
Variable Importance Rank
MambaUNet
MambaUNetC
SwinUNet
SwinUNetC
UNet
Feature Space

Figure 13